Energy & Environmental Science

REVIEW

View Article Online
View Journal | View Issue

Cite this: *Energy Environ. Sci.*, 2014, **7**, 2182

Inorganic-modified semiconductor TiO_2 nanotube arrays for photocatalysis

Mengye Wang,[ab] James Ioccozia,[b] Lan Sun,*[a] Changjian Lin*[a] and Zhiqun Lin*[b]

Received 15th January 2014
Accepted 14th April 2014

DOI: 10.1039/c4ee00147h

www.rsc.org/ees

Semiconductor photocatalysis is a promising physicochemical process for the photodegradation of organic contaminants and bacterial detoxification. Among various oxide semiconductor photocatalysts, TiO_2 has garnered considerable attention because of its outstanding properties including strong oxidizing activity, chemical and mechanical stability, corrosion resistance, and nontoxicity. This Review briefly introduces the key mechanisms of photocatalysis, highlights the recent developments pertaining to pure TiO_2 nanotube arrays and TiO_2 nanotube arrays modified by non-metals, metals and semiconductors, and their applications in the photocatalytic degradation of organic dyes. The improved photocatalytic efficiencies of modified TiO_2 nanotube arrays are compared with unmodified counterparts. Current challenges and prospective areas of interest in this rich field are also presented.

Broader context

Research on earth-abundant and environmentally benign nanomaterials for photocatalytic or photoelectrochemical degradation of organic pollutants, the splitting of water into H_2, and solar cells holds promise for meeting the global challenge of supplying clean energy. In this context, semiconductor TiO_2 stands out as one of the most widely studied nanomaterials because of its attractive attributes, including strong oxidizing ability to decompose organic pollutants, nontoxicity and low cost. In this Review, recent advances in the utilization of pure TiO_2 nanotube arrays and TiO_2 nanotube arrays modified by non-metals, metals and semiconductors for photocatalytic degradation of organic dyes are highlighted. Current challenges and prospects for the future research direction in this field are provided.

1. Introduction

Serious environmental pollution and depletion of fossil fuel resources have emerged as two major obstacles for the sustainable development of human society. The textile dyeing industry, releasing non-biodegradable organic pollutants into the ecosystem, is a serious threat to the environment. Therefore, it is imperative to develop green and efficient technologies to control and reduce pollution growth. Traditional techniques, such as adsorption, precipitation and reverse osmosis, simply transfer pollutants from one phase to another or concentrate them in one phase instead of actually degrading them.[1–4] In recent years, photocatalysis using anatase titanium dioxide (TiO_2) has become a promising route to degrade organic pollutants.[5–8] TiO_2 is one of the most widely used photocatalytic materials due to its exceptional ability to oxidatively decompose organic pollutants, corrosion resistance, durability, nontoxicity and low cost.[5,9–21] Many studies have focused on synthesizing TiO_2 with various structures (*e.g.* nanotube arrays, nanoparticles, nanorods, mesoporous spheres, multichannel microtubes, nanosheets, nanowires, micro-flowers, flower clusters *etc.*), some of which are shown in Fig. 1.[22–30] Among them, highly ordered TiO_2 nanotube arrays (NTAs), standing vertically on the Ti substrate, appear to be an ideal form for promoting photocatalysis.[31] Hence, the focus of this Review will be specifically TiO_2 nanotube arrays and their application in

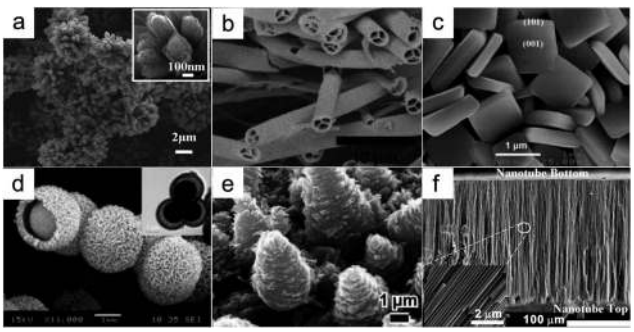

Fig. 1 SEM images of TiO_2. (a) Flower-like clusters, (b) multichannel microtubes, (c) nanosheets, (d) mesoporous spheres, (e) micro-flowers, and (f) nanotube arrays. Adapted with permission from ref. 22–24, 27, 29 and 30, Copyright© 2007, 2008, 2009 American Chemical Society, 2011 IOPscience and 2013 Wiley-VCH.

[a]*Department of Chemistry, College of Chemistry and Chemical Engineering, and State Key Laboratory of Physical Chemistry of Solid Surfaces, Xiamen University, Xiamen, Fujian 361005, PR China. E-mail: sunlan@xmu.edu.cn; cjlin@xmu.edu.cn*

[b]*School of Materials Science and Engineering, Georgia Institute of Technology, Atlanta, GA 30332, USA. E-mail: zhiqun.lin@mse.gatech.edu*

photocatalytic degradation processes. When compared with other TiO_2 structures, NTAs with smooth surfaces possess advantageous one-dimensional geometry[32–34] for efficient charge transfer. This improved configuration affords significantly shorter carrier-diffusion paths along the tube walls and thereby minimizes the occurrence of charge losses due to the electron hopping between nanoparticles.[35,36] In comparison with freestanding NTAs, NTAs formed from the Ti substrate not only can be recycled more readily, but also can be utilized as an electrode. When a small bias potential is applied, the NTA electrode can achieve high photoelectrocatalytic efficiency. The most studied forms of TiO_2 NTAs are anatase and rutile.[37–41] Compared to the rutile form, the anatase structure possesses higher photocatalytic activity.[39,40] In this Review, TiO_2 refers to the anatase form unless otherwise noted.

Although the favorable characteristics of TiO_2 NTAs are apparent, several disadvantages are also worth noting. A wide bandgap (3.2 eV) prevents TiO_2 NTAs from achieving more extensive usage. Due to its large bandgap, TiO_2 NTAs require UV light irradiation for photocatalytic activation. Since UV light accounts for a small portion (5%) of the solar spectrum as compared to visible light (52%) and infrared light (43%), any shift in optical-response of TiO_2 NTAs toward the longer wavelength region gives the possibility of higher photocatalytic activity. In addition, fast recombination of photoinduced electron–hole pairs limits photocatalytic efficiency of TiO_2 NTAs. These two disadvantages must be addressed in order to enhance the photocatalytic activity of TiO_2 NTAs and will be of key interest throughout this Review.

Various strategies have been explored in order to address the disadvantages of TiO_2 NTAs noted above. These strategies can be grouped into three principle methods. The first method involves doping of a non-metal (N, B, P, *etc.*) into the TiO_2 NTAs

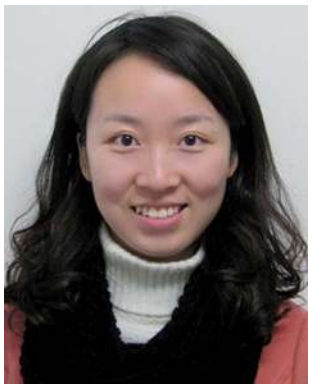

Mengye Wang is a Ph.D. student in the College of Chemistry and Chemical Engineering at Xiamen University. She received her Bachelor of Science in Chemistry from Xiamen University in 2010. She is currently a visiting Ph.D. student in Prof. Zhiqun Lin's group at the Georgia Institute of Technology. Her research interests include advanced materials in photocatalytic degradation of organic pollutants, water splitting and dye-sensitized solar cells.

James Iocozzia is a graduate student in the School of Materials Science and Engineering at the Georgia Institute of Technology. He received his Bachelor of Science in Polymer and Fiber Engineering from the Georgia Institute of Technology in 2012. His research interests include liquid crystals, nanocomposites and block copolymers. He is a Graduate Student Presidential Fellow, and BIONIC Scholar.

Lan Sun is an Associate Professor in the College of Chemistry and Chemical Engineering at Xiamen University. She received her Ph.D. in Materials Science and Engineering from Tsinghua University in 2002. Her research interests include semiconductor nanocomposites, semiconductor photoelectrochemistry, advanced materials for environmental and energy application, such as photocatalytic degradation of organic pollutants, water splitting hydrogen production and dye-sensitized solar cells.

Changjian Lin is a Professor in the State Key Laboratory of Physical Chemistry of Solid Surfaces, and College of Chemistry and Chemical Engineering at Xiamen University. He received his Ph.D. in Physical Chemistry from Xiamen University in 1985. His research interests include electrochemical methods, corrosion and protection, biomaterials and biosurfaces, advanced materials for energies and environments, such as dye-sensitized and quantum dots-sensitized solar cells, photogenerated cathodic protection, surface wettability, water splitting hydrogen production and photocatalytic degradation of organic pollutants.

Zhiqun Lin is a Professor in the School of Materials Science and Engineering at Georgia Institute of Technology. He received his Ph.D. in Polymer Science and Engineering from University of Massachusetts, Amherst in 2002. His research interests include polymer solar cells, dye-sensitized solar cells, semiconductor organic–inorganic nanocomposites, photocatalysis, quantum dots (rods), conjugated polymers, block copolymers, polymer blends, hierarchical structure formation and assembly, surface and interfacial properties, multifunctional nanocrystals, and Janus nanostructures. He is a recipient of an NSF Career Award.

crystal lattice. The non-metal replaces O^{2-} or Ti^{4+} and creates new energy levels, thus narrowing the bandgap of TiO_2 NTAs.[5,42–49] The second strategy is to decorate TiO_2 NTAs with a metal. There are two mechanisms for metal decoration that can improve the photocatalytic performance of TiO_2 NTAs. One mechanism involves doping with metals, such as Fe, Zr and Cr, which narrows the bandgap by replacing Ti^{4+} in TiO_2 NTAs and generating sub-energy levels.[18,50–53] The other mechanism takes advantage of the high work function of noble metals (Pd, Au, *etc.*) to facilitate the electron transfer from TiO_2 NTAs to noble metal, which significantly reduces the recombination of photogenerated electron–hole pairs in TiO_2 NTAs.[15,19,20,54–61] The surface plasmon resonance (SPR) effect of noble metals could also contribute to higher photocatalytic efficiency of TiO_2 NTAs.[15,61] Third, a narrow bandgap semiconductor (CdS, Cu_2O, *etc.*), whose conduction band (CB) is higher than that of TiO_2 NTAs, can act as a sensitizer when coupled with TiO_2 NTAs.[17,21,62–65] Under light irradiation, photoinduced electrons would transfer from the CB of the narrow bandgap semiconductor to that of TiO_2 NTAs, and thus enhance the photocatalytic efficiency.

The photocatalytic properties of TiO_2 are derived from the formation of photoinduced charge carriers consisting of holes and electrons when ultraviolet (UV) light corresponding to the bandgap of 3.2 eV is absorbed.[6,66–68] The primary mechanism of photocatalysis can be represented by eqn (1)–(7).[69]

$$TiO_2 + h\nu \rightarrow h_{VB}^{+} + e_{CB}^{-} \quad (1)$$

$$e_{CB}^{-} + >Ti^{IV}OH \rightarrow [>Ti^{III}OH] \quad (2)$$

$$h_{VB}^{+} + >Ti^{IV}OH \rightarrow [>Ti^{IV}OH^{\bullet}]^{+} \quad (3)$$

$$e_{CB}^{-} + [>Ti^{IV}OH^{\bullet}]^{+} \rightarrow >Ti^{IV}OH \quad (4)$$

$$h_{VB}^{+} + [>Ti^{III}OH] \rightarrow >Ti^{IV}OH \quad (5)$$

$$[>Ti^{IV}OH^{\bullet}]^{+} + red \rightarrow >Ti^{IV}OH + red^{\bullet+} \quad (6)$$

$$[>Ti^{III}OH] + Ox \rightarrow Ox^{\bullet} \quad (7)$$

where h_{VB}^{+} is a valence-band hole, e_{CB}^{-} is a conduction-band electron, >TiOH represents the primary hydrated surface functionality of TiO_2, red is an electron donor (*i.e.*, reductant), and Ox is an electron acceptor (*i.e.*, oxidant).[69]

As previously mentioned, TiO_2 possesses a wide bandgap, which extends from the top of the filled valence band (VB) formed by the overlap of oxygen 2p orbitals to the bottom of the vacant conduction band (CB) formed by the 3d orbital of Ti^{4+}. Under light irradiation with energy equal to or greater than the bandgap of TiO_2, electrons are excited from the VB to the CB and holes are left at the VB (eqn (1)). After the separation of photogenerated electron–hole pairs, electrons and holes move to the surface of TiO_2. Photoinduced electrons are captured by the surface hydroxyls (>Ti^{IV}OH) to form surface-trapped CB electrons [>Ti^{III}OH] (eqn (2)), and then donated to reduce electron acceptors (*i.e.*, O_2, bubbled into the solution) (eqn (7)). Thus, superoxide radical anions ($^{\bullet}O_2^{-}$) are generated and undergo reactions with H_2O to yield OH^{-} or combine with H^{+} to form hydrogen peroxide (H_2O_2).[70] Subsequently, H_2O_2 reacts with $^{\bullet}O_2^{-}$ and is reduced to hydroxyl radicals $^{\bullet}OH$ and OH^{-}.[70] Complex reactions can also occur between these intermediates and the organic pollutant adsorbed on TiO_2 to produce $^{\bullet}O_2^{-}$, which would go through the reactions above. Photoelectrocatalysis is more efficient if the pollutant is preadsorbed on TiO_2 NTAs.[71] Meanwhile holes react with >Ti^{IV}OH to form surface-trapped valence-band holes [>$Ti^{IV}OH^{\bullet}$]$^{+}$ (*i.e.*, $^{\bullet}OH$) (eqn (3)), which diffuse to the TiO_2 surface to oxidize electron donor species (eqn (6)). Nevertheless, photoinduced electron–hole recombination competes with the charge transfer process. Recombinations can occur within the TiO_2 NTAs (eqn (4) and (5)) or on the surface with the release of heat. The strong oxidizing activity of $^{\bullet}OH$ can mineralize almost all the organic pollutants to non-hazardous final products. The entire photocatalytic degradation process, using TiO_2 as a photocatalyst, is illustrated in Fig. 2.

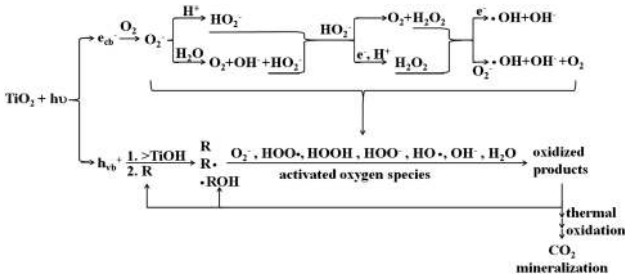

Fig. 2 Photocatalytic degradation process utilizing TiO_2. Adapted with permission from ref. 69, Copyright© 1995 American Chemical Society.

The immense volume of research on TiO_2-based materials necessitates a closer look at specific systems and combinations in detail. To that end, this Review, for the first time, will focus solely on the state-of-the-art in TiO_2 NTAs and their application in the photocatalytic degradation of pollutants. This Review briefly discusses the mechanism of photocatalysis as noted in Section 1. The application of highly ordered nanotube arrays for photocatalytic degradation of organic pollutants, concentrating primarily on current decoration techniques, is presented in Section 2. Finally, a perspective on future areas and challenges facing the design and improvement of TiO_2 NTA photocatalysts is provided in Section 3. This Review is intended to serve as a reference for established researchers as well as unfamiliar parties interested in the broad field of TiO_2 photocatalysis.

2. Photocatalytic degradation of dyes

2.1 Pure TiO_2 nanotube arrays for photocatalytic degradation

In the activation or diffusion-controlled photocatalytic process, TiO_2 NTAs exhibit better catalytic performance than TiO_2 nanoparticle films. This is attributed to several reasons previously detailed.[31,66,72] First, the long axis of TiO_2 NTAs offers a direct pathway for carrier transport,[31] thereby lowering the trapping and recombination kinetics of photoinduced electron–

hole pairs. This contrasts sharply to the traveling (*i.e.*, hopping) of electron–hole pairs between nanoparticles as in the case of nanoparticle films.[66] Moreover, the nanotube geometry also shortens the diffusion path between degradation compounds in solution and the active surface area of nanotubes, whereas the porous structure of nanoparticles imparts longer diffusion lengths.[66]

The effects of critical structure factors of TiO_2 NTAs photocatalytic activity have also been explored. Zhuang *et al.* studied the effect of TiO_2 nanotubes with different film thicknesses (*i.e.*, 0.4, 1.5, 2.5, 3.1 and 3.5 μm) and tube diameters (*i.e.*, 55, 100 and 125 nm) on the photocatalytic degradation of methyl orange (MO).[73] It was found that the film thickness of nanotube arrays had a profound influence on the photocatalytic efficiency as a result of its surface area and the separation efficiency of photogenerated electron–hole pairs within the nanotube arrays. As a result, the 2.5 μm-thick film possessed the highest photocatalytic efficiency. However, the tube diameter for a given nanotube length was shown to exert only a marginal effect on photocatalytic activity. It is possible that as the diameter of nanotubes increases, the decreased surface area to volume ratio of TiO_2 NTAs would result in a negative effect on photocatalytic efficiency, while the increased light transmittance with the increased pore size of TiO_2 NTAs would improve photocatalytic activity.

It is worth noting that the photocatalytic degradation rate is strongly dependent on the electrolyte composition, anodization voltage and anodizing time.[11,74,75] The structure and morphology of nanotube layers depend largely upon these three factors as well. Compared to inorganic electrolytes, the diffusion of fluorine ion is confined in the electrolyte-containing organic phase (*e.g.*, glycerol), which slows the process of electrochemical etching of titanium.[74] The optimized volumetric ratio of glycerol to deionized water needed to efficiently yield nanotube array films was between 1 : 1 and 2 : 1.[74,76] The nanotube diameters and thicknesses varied linearly[74] over a particular range of applied voltages (for example, from 1 V to 25 V (ref. 77)), beyond which only porous structures were obtained.[74] The thickness of nanotube membranes was also found to be affected by the anodization time.[74] The thickness first increased sharply and thereafter the growth rate decreased. When the dissolution rate of nanotubes equals the rate of inward movement of the metal oxide interface, the thickness of nanotubes reaches a plateau.[74] Under the appropriate electrolyte composition and electrochemical conditions, TiO_2 NTAs can be rapidly fabricated with an adjustable diameter from 15 to 150 nm and a thickness from a few nanometers to several micrometers, and thus the effect of these parameters on photocatalysis can be elucidated as noted above.[73]

The posttreatments (*i.e.*, vapor-thermal treatment, hydrothermal treatment, and calcination) can also heavily influence the photocatalytic activity of TiO_2 NTAs.[78] For example, well-aligned nanotube arrays of approximately 2.1 μm length are completely destroyed by the hydrothermal treatment at 180 °C and only aggregated anatase particles are observed.[78] Conversely, the calcination at 450 °C had no influence on the surface morphology and architecture of TiO_2 NTAs.[78] The vapor-treated TiO_2 NTAs showed the highest photocatalytic activity because of good crystallization and the retention of tubular structures.[78] The calcination of TiO_2 NTAs at different temperatures had a great effect on photocatalytic activity.[11,74,75] Yu *et al.* found that for a membrane with a thickness of approximately 1.9 μm, photocatalytic efficiency increased rapidly as the calcination temperature increased from 300 °C to 600 °C due to the formation of the anatase structure and enhanced crystallization.[75] At 600 °C, the sample showed the maximum photocatalytic activity as a direct consequence of the bi-phase structure (*i.e.*, anatase and rutile), improved crystallization, and the retention of tubular structures. However, a great reduction in the photocatalytic efficiency occurred at higher temperature calcinations (*i.e.*, 700–800 °C) due to the formation of the rutile phase, the collapse of tubular structures, and the decrease of surface area.

Recently, novel tube-in-tube TiO_2 NTAs with coarse porous walls were obtained by a one-step anodization process.[79] This architecture substantially increased the surface area of nanotube arrays. In the photocatalytic degradation of Methylene Blue (MB), three structure domains: the internal and external tube surfaces together with the area between the two coarse subshells within the tube were available. This led to markedly increased adsorption of organic dyes and improved degradation rates.

2.2 Modified TiO_2 nanotube arrays for photocatalytic degradation

2.2.1 TiO_2 nanotube arrays modified with non-metals. Non-metal ion doping into the TiO_2 lattice replaces some oxygen vacancies to form $TiO_{2-x}A_x$ (where A represents a non-metal, such as N, S, B, F or P) and induce new energy levels located near the band edges or as mid-gap states that may reduce the effective bandgap of TiO_2 NTAs and extend the photoactive region.[5] This kind of doping should meet the following requirements:[5] (i) the doping should generate energy states in the bandgap of TiO_2 in order to absorb visible light; (ii) the conduction minimum of doped TiO_2, including subsequent impurity states, needs to be as high as that of undoped TiO_2 to ensure its photocatalytic activity; and (iii) the states in the bandgap of doped TiO_2 must sufficiently overlap with the band states of undoped TiO_2 to transfer photogenerated carriers to reactive sites on the TiO_2 surface. Several non-metal dopants are considered in this section. Both the relative size and electronic structure of the non-metals dictate the degree of enhancement or inhibition of properties as well as confer unique and particular properties. Both the general and specific benefits and drawbacks are addressed in this section.

The substitutional doping by N is found to be the most effective as its p orbital states lead to bandgap narrowing by mixing with the O 2p states. This is supported by calculating density of states for substitutional doping of C, N, F or S for O into the lattice of anatase TiO_2 crystals.[5] The distinct shift of the absorption edge towards lower energy has been observed by photoinduced electrons transferring from N $2p_\pi$ to Ti d_{xy}, instead of from O $2p_\pi$ as in TiO_2.[80] Recently, N-doped TiO_2 NTAs

have been fabricated by a simple wet immersion method.[81] As shown in Fig. 3a, the photocurrent of modified samples depended strongly on the annealing temperature. The photocurrent first increased significantly with the calcination temperature, and a maximum was achieved for the sample annealed at 450 °C as the phase changed from amorphous to anatase. Further increasing the annealing temperature resulted in a decline in photocurrent. A shift of the photocurrent peak to higher wavelengths was observed. This is not surprising as annealing at temperatures higher than 450 °C induced a phase change from anatase to rutile, which has a narrower bandgap of approximately 3.0 eV (Fig. 3a). This transition process was accompanied by either thicker nanotube walls or the destruction of nanotube array structures. The N-doped TiO_2 NTAs calcined at 450 °C had the highest photocatalytic degradation rate of the methylene orange (MO) pollutant (Fig. 3c and d) and remained stable after a 10-cycle repetition in photocatalysis (Fig. 3b). Compared to undoped TiO_2 NTAs, the degradation rate of N-doped TiO_2 NTAs was improved by 74.7% and 14.1% under UV and visible irradiation, respectively. Interestingly, the liquid phase deposition method was also developed to dope TiO_2 NTAs with N, and enhanced absorption of N-doped TiO_2 NTAs under visible light was observed.[82] Consequently, the degradation of methylene blue (MB) was enhanced by 50% and 200% under the UV and visible irradiation, respectively. Notably, N_2-plasma[83] and dip-calcination[84] methods were also employed to yield N-doped TiO_2 NTAs, and their corresponding photocatalytic activities were improved (Table 1).

It should be noted that doping with S exhibits a similar bandgap narrowing as with N. However, it is more difficult to incorporate it into the lattice of TiO_2 crystals due to its larger ionic radius.[5] When TiO_2 NTAs were treated with thiourea and then calcined under vaccum,[85] it was found that N existed in the forms of N–Ti–O and N–O–Ti, while S substituted O, forming a Ti–S bond.[85] Compared with undoped TiO_2 NTAs, N–S-codoped TiO_2 NTAs exhibited improved crystallinity and optical absorption, and thus better photocatalytic activity. Interestingly, a C–N-codoped TiO_2 NTAs/carbon nanorod heterojunction photocatalyst was fabricated by chemical vapor deposition (CVD).[45] The C–N doping shifted the absorption edge of TiO_2 NTAs to the visible light region and the carbon nanorods promoted the charge carrier transfer from the TiO_2 surface to the electrolyte. As a result, the degradation rate of modified TiO_2 NTAs was twice that of the undoped NTAs.

Continuing along the row to larger atoms, boron can also serve as a useful non-metal dopant in TiO_2 NTAs. Boron oxides at the surface and grain boundaries as well as in the matrix of TiO_2 can easily be incorporated into the framework of Ti and hence promote an increase in surface defects (*i.e.*, oxygen vacancies).[86] This is because the ionic radius of B^{3+} (0.023 nm) is smaller than that of Ti^{4+} (0.064 nm). B-doped TiO_2 NTAs have been prepared by the CVD method utilizing trimethyl borate as the boron source and N_2 as the carrier gas.[46] It is believed that the B atom is incorporated into TiO_2, and the chemical environment surrounding B is likely Ti–B–O. The noteworthy photoconversion efficiencies of B-doped TiO_2 NTAs were found to be 31.5% and 15.1% under the high-pressure mercury lamp irradiation and $\lambda > 290$ nm light irradiation, respectively. It was demonstrated that the photoelectrochemical degradation efficiency of pentachlorophenol (PCP) by the B-doped TiO_2 NTAs was 43.4% and 67.4% higher than that of the undoped systems under UV and visible light, respectively. Boron can also be doped into the lattice of TiO_2 by electrodeposition and potentiostatic anodization.[87,88] A sample with 3.1 atom% of boron was found to exhibit the best photochemical properties, and its photocurrent densities under simulated sunlight and UV irradiation were approximately 1.17 and 1.27 times of those of pure TiO_2 NTAs, respectively.[88]

Recently, B–N-codoped TiO_2 NTAs were prepared in an electrolyte containing BF_3 *via* an anodization process, followed by annealing in ammonia at 500 °C.[49] The synergistic effects of B and N were demonstrated by photocatalytic and photoelectrochemical performances of B–N-codoped TiO_2 NTAs. The mechanism of the B–N co-doping effect is elaborated below.[89] The Ti–O–B–N moiety acts as a photocatalytic "hot site" to promote surface separation and transfer of carriers by trapping holes. This is due to the localized nature of the Ti–O–B–N states, contributing to a more effective physical separation of surface reduction and oxidation reactions by minimizing the state overlap that would otherwise lead to electron–hole recombination.

In addition to doping into the lattice of TiO_2, B can be doped with diamond to form p-type boron-doped diamond (BDD).[90] It is desirable to combine TiO_2 NTAs with BDD by a liquid phase deposition method using a ZnO nanorod template to form n-type TiO_2/p-type BDD heterojunctions that possess high photocatalytic activity with good recycle behavior.[90]

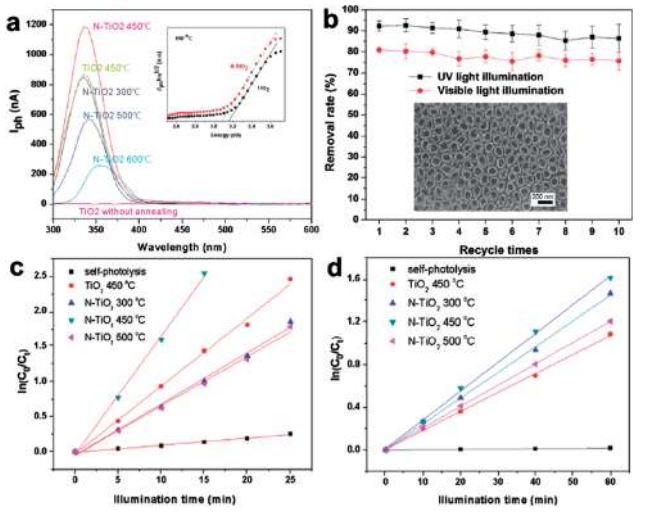

Fig. 3 (a) Photocurrent of TiO_2 NTAs with and without thermal annealing as well as N-doped TiO_2 NTAs annealed at different temperatures. (b) Recycling test of N-doped TiO_2 NTAs. The inset shows the SEM image of N-doped TiO_2 NTAs after a ten-repeat-cycle test. Comparison of photocatalytic activity of pure TiO_2 NTAs and N-doped TiO_2 NTAs annealed at different temperatures under (c) UV light irradiation, and (d) visible light irradiation, respectively. Adapted with permission from ref. 81, Copyright© 2010 Elsevier.

Table 1 Methods for forming non-metal-modified TiO_2 NTAs and the corresponding photocatalytic performance

Non-metal	Methods	Light source	Pollutants to be degraded	Improved photocatalytic efficiency as compared to unmodified system (%)	Ref.
N	Wet immersion	UV	MO	74.7[a]	81
		Visible		14.1[a]	
	Liquid phase deposition,	UV	MB	50.0[b]	82
		Visible		200.0[b]	
	N_2-plasma,	Visible	MB	157.1[a]	83
	Dip-calcination	Visible	X–3B	344.4[a]	84
B	CVD	UV	PCP	43.4[a]	46
		Visible		67.4[a]	
	Anodization	Visible	Atrazine	53[a]	88
	Electrodeposition	Visible	Phenol	28[a]	87
F–B	CVD	Visible	MO	482.6[b]	92
N–S	Heat treatment	Visible	MB	24.5[b]	85
C–N	CVD	Visible	MO	101.2[b]	45
N–F	Anodization	UV	MO	63.5[a]	93

[a] The number was calculated by $(r_m - r_{unm})/r_{unm}$, where r_m and r_{unm} are apparent rate constants deduced from the slope of linear fitting of $\ln(C_0/C)$ *versus* reaction time using modified TiO_2 NTAs and unmodified TiO_2 NTAs, respectively. C_0 and C are initial and reaction concentrations of the targeted pollutant, respectively. [b] The number was calculated by $(C_{unm} - C_m)/C_{unm}$, where C_m and C_{unm} are the concentrations of the targeted pollutant which was degraded for a certain period of time by using modified TiO_2 NTAs and unmodified TiO_2 NTAs, respectively.

Similarly, F-doping can result in the creation of surface oxygen vacancies[91] and has been widely used in co-doping. Su *et al.* employed CVD to simultaneously co-dope F and B into TiO_2 NTAs.[92] The small ionic radius of F allows it to be easily incorporated into the lattice. After being annealed at 600 °C, the F–B-co-doped samples displayed strong absorption in both UV and visible wavelength ranges, and exhibited the clearest cooperative effect of F and B on the enhancement of photocurrents and PEC activity. N–F-co-doped TiO_2 NTAs were recently obtained *via* electrochemical anodization.[93] A noteworthy synergy between the photocatalytic and electrochemical processes was evidenced due to the use of high-aspect-ratio TiO_2 NTAs and the favorable impact of N and F co-doping on the photocatalytic performance.[93]

Phosphorus species have attracted increasing interest because of their ability to stabilize mesoporous structures and improve the photocatalytic activity.[94] Therefore, it is expected that P-doping TiO_2 NTAs will improve the shifting of their optical response to the visible range. P-doped TiO_2 NTAs can be synthesized by anodization processes.[95,96] A significant red shift of the absorption edge was observed for doped samples, which was attributed to the introduction of P^{5+} into TiO_2 crystal lattices which partially replaced Ti^{4+} and the possible impurity energy level formed in the TiO_2 bandgap.[96] However, P-doped TiO_2 NTAs possessed much lower catalytic activity than pure TiO_2 NTAs.[95] The amorphous impurities containing phosphorus in the P-doped TiO_2 NTAs are the principle cause for the poor performance as they act as recombination centers for photoinduced charges which scavenge photogenerated holes.

In most cases, non-metals are efficiently doped into the lattice of TiO_2 where they substitute oxygen vacancies while preserving the highly organized nanotubular structure of TiO_2 NTAs, which facilitates the transfer of charge carriers. The non-metal-doped TiO_2 NTAs exhibit red shifts in their absorption edge and enhanced absorption in the visible region. The methods for non-metal doping of TiO_2 NTAs and the corresponding photocatalytic performances are summarized in Table 1. It is clear that the increase in photocatalytic efficiency for traditional non-metal doping (*i.e.*, B-, C-, N- and F-doped) is usually less than 150% when compared with pure TiO_2 NTAs (Table 1). After doping with N (ref. 84 and 97) and B (ref. 46), the bandgap of TiO_2 NTAs can be reduced by at most 0.3 eV. This is because of the limited number of energy levels of non-metals that can be induced within the TiO_2 bandgap. Therefore, the significant enhancement in visible light absorption remains a great challenge for doping with non-metals.

2.2.2 TiO_2 nanotube arrays decorated with metals

2.2.2.1 TiO_2 nanotube arrays decorated with metal ions. Decorating TiO_2 with transition metal ions and rare earth metal ions has been widely recognized as a route to expand the photoresponse of TiO_2 nanoparticles into the visible light spectrum.[98–104] This is attributed to the incorporation of metal ions into the TiO_2 lattice. The extrinsic energy levels in the bandgap of TiO_2 are formed and can be described as follows:[105]

$$M^{n+} + h\nu \rightarrow M^{(n+1)+} + e_{CB}^{-} \quad (8)$$

$$M^{n+} + h\nu \rightarrow M^{(n-1)+} + h_{VB}^{+} \quad (9)$$

where M and M^{n+} represent the metal and the metal ion dopant, respectively. It should be noted that electron or hole transfer between metal ions and TiO_2 can decrease the rate of photogenerated electron–hole recombination. The reduction energy level of metal ions should be less negative than the CB edge of TiO_2, while the oxidation energy level of metal ions should be less positive than the VB edge of TiO_2. Furthermore, metal ion dopants must be near the surface of TiO_2 NTAs for improved charge transfer. Several different metal ion dopants are

addressed herein with particular attention given to both improvements and technical/practical challenges to their use.

Among all available metal candidates, Fe is one of the most suitable substances for industrial photocatalytic applications due to its low cost. Doping TiO_2 with Fe ions is an effective approach to enhance the response to visible light and increase photocatalytic efficiency for two reasons. One is the charge transfer transition from 3d electrons of Fe^{3+} to the CB of TiO_2.[106,107] The second is the d–d transition of Fe^{3+} ($^2T_{2g} \rightarrow {}^2A_{2g}$, $^2T_{1g}$) and the charge transfer transition between Fe ions ($Fe^{3+} + Fe^{3+} \rightarrow Fe^{4+} + Fe^{2+}$).[107,108] Several strategies for incorporating Fe ions into the TiO_2 lattice are considered here. Since the radius of Fe ions is close to Ti^{4+}, Fe ions can be easily incorporated into the TiO_2 lattice. Fe^{3+}-doped TiO_2 NTAs were recently prepared by electrochemical anodization in an HF electrolyte containing Fe ions.[52] Fe^{3+}-doped TiO_2 NTAs displayed increased photocurrent and red shift of the optical absorption edge. The ideal concentration of doped Fe^{3+} was found to be approximately 0.1 M derived from $Fe(NO_3)_3$. With this amount of Fe^{3+}, TiO_2 NTA photocatalysts showed the highest removal rate of MB under UV irradiation: 81.0% higher than the pristine TiO_2 NTAs. As shown in Raman spectra, as the amount of Fe^{3+} increased, the peak was broadened. This was due to Fe^{3+} doping into the crystal lattice of TiO_2, leading to structural changes in the lattice and the cleavage of the vibration phonon modes. Fe-doped TiO_2 NTAs were also prepared by an impregnating-calcination method using $Fe(NO_3)_3$ as the precursor.[53] 0.5 M Fe modification was found to maximize the enhancement of photocurrent and PEC activity of samples, exceeding those of pure TiO_2 NTAs by a factor of approximately 10 and 2.5, respectively, at a bias potential of 0.4 V under visible light irradiation.[53] Similarly, Fe-modified TiO_2 NTAs can be produced by an ultrasound-assisted impregnating-calcination method.[18] It was demonstrated that α-Fe_2O_3 nanoparticles with 10–20 nm in diameter were deposited inside the TiO_2 nanotubes (Fig. 4a) while Fe ions were doped into the TiO_2 lattice. The absorption of samples in the visible light range was found to increase with increasing Fe content (Fig. 4b). The highest degradation efficiency of MB was obtained using the Fe-modified TiO_2 NTA samples prepared by pre-sonicating for 5 min and annealing at 500 °C. Photoluminescence (PL) (Fig. 4c) and electrochemical impedance spectroscopy (EIS) measurements (Fig. 4d) further support that Fe-modification effectively promotes the separation and transfer of charge carriers, which was responsible for the enhanced photocatalytic activity.[18] The Fe–TiO_2 NTAs photocatalyst remained stable after 8-photocatalytic-cycle runs.

Similar to Fe, Cr can be doped into the lattice of TiO_2 as well. Intriguingly, Cr-doping can also prevent the anatase phase of TiO_2 from converting to the rutile phase under high temperature.[50] Cr-doped TiO_2 NTAs were prepared by electrochemical oxidation in glycerol/fluoride electrolyte solution with potassium dichromate as the Cr source.[50] Cr-doping prevented the anatase phase of TiO_2 from converting to the rutile phase under high temperature. Cr-doped TiO_2 NTAs showed higher photocurrent than undoped TiO_2 NTAs, depending on the Cr source concentration and annealing temperature. The optimal concentration of Cr and annealing temperature were found to

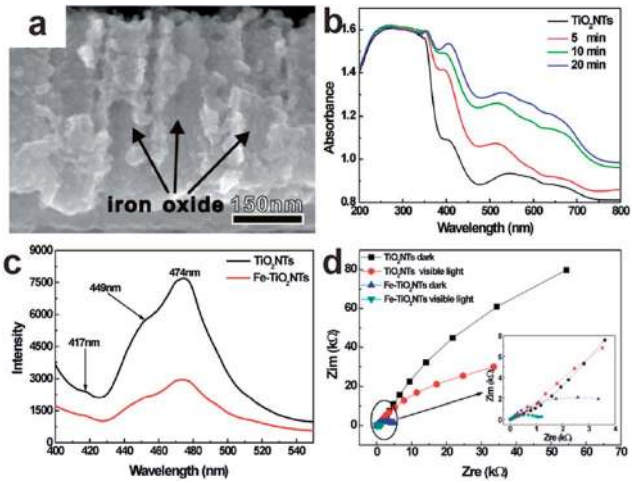

Fig. 4 (a) SEM image of Fe-modified TiO_2 NTAs obtained after ultrasonication for 20 min. (b) Diffuse reflectance spectra of TiO_2 NTAs and Fe-modified TiO_2 NTAs prepared at different ultrasonication times. (c) PL spectra of TiO_2 NTAs and Fe-modified TiO_2 NTAs. (d) Nyquist plots of TiO_2 NTAs and Fe-modified TiO_2 NTAs prepared for 5 min in the dark and under visible light irradiation. A close-up of circle in (d) is shown as the inset. Adapted with permission from ref. 18, Copyright© 2012 Elsevier.

be 0.015 M and 400 °C, respectively. The modified photocatalyst exhibited high PEC activity in degrading MO, and the MO removal rate remained almost unchanged after five PEC degradation cycles.

Unlike those of Fe and Cr which are smaller than Ti, the atomic radius of Zr is slightly larger than that of Ti. However, Zr can still be easily introduced into the TiO_2 lattice. In particular, when Zr is doped into the TiO_2 lattice, the lattice strain will be increased. To alleviate this strain, the lattice oxygen, especially surface oxygen, escapes from the lattice and exists as a hole trap. Thus, the photocatalytic performance will be enhanced. By employing an electrochemical process using 0.1 M $Zr(NO_3)_4$ as the Zr source, followed by calcination, Zr-doped TiO_2 NTAs can be fabricated.[51] The calcination process facilitated the incorporation of Zr into the TiO_2 lattice. The Zr-doped TiO_2 NTAs displayed higher photocatalytic efficiency in degrading Rhodamine B (RhB) under UV irradiation than pure TiO_2 NTAs. The Zr-doped TiO_2 NTA photocatalysts obtained at 7 V and calcined at 600 °C possessed the highest degradation rate (*i.e.*, 54.7% higher than pure TiO_2 NTAs), where the optimal ratio of Zr/Ti was found to be 0.047. Interestingly, this photocatalyst can be used more than 20 times and its degradation rate remained virtually unchanged. The improved photocatalytic activity of Zr-doped TiO_2 NTAs can be attributed to the following two reasons. First, it is induced by increased lattice strain caused by similar ionic radius. Second, Zr-doping can induce new defects in the TiO_2 matrix, which allows electron trapping on Zr^{4+} rather than Ti^{4+}. The defects reduce charge recombination and improve photocatalytic activity.[109,110] Recently, N–Zr-co-doped TiO_2 NTAs were obtained through an electrochemical approach in an electrolyte containing $Zr(NO_3)_4$ and NH_4Cl.[111] It was found that N and Zr significantly improved the photocatalytic efficiency of TiO_2 NTAs under both UV and visible light irradiation.

After metal-ion decoration, the morphology of TiO_2 NTAs is retained. The photocatalytic efficiency is improved after metal-ion decoration due to the introduction of new energy levels or defects. There exists an optimum concentration for each metal ion dopant, beyond which photocatalytic activity decreases due to an increase in the electron–hole recombination. The methods for metal-ion decoration of TiO_2 NTAs and the corresponding photocatalytic performance are summarized in Table 2. In comparison to undoped TiO_2 NTAs, the increase in photocatalytic efficiency for metal-ion-decorated TiO_2 NTAs is typically less than 100% (Table 2). The challenge for such devices is identifying and optimizing the necessary doping ion or ions to confer the enhanced performance over a desired temperature range as well as the sufficient longevity of the resulting photocatalysts. The abundance and readily available precursors for such dopants make them highly attractive for large volume, low cost photocatalysts.

2.2.2.2 TiO_2 nanotube arrays loaded with noble metals. Precious metals usually have high work functions. When TiO_2 NTAs are loaded with noble metals, photoinduced electrons quickly transfer from TiO_2 to noble metals, participating in a reduction reaction. Meanwhile, the holes move to the TiO_2 surface to take part in an oxidation reaction. Therefore, noble-metal-loaded TiO_2 NTAs render efficient separation of photogenerated charge carriers, and thus increase the overall photocatalytic efficiency. Owing to the surface plasmon resonance (SPR) of noble metals, noble-metal-loaded TiO_2 NTAs often possess higher photocatalytic efficiency when compared to pure NTAs.[15,56] It should be noted that the effect of SPR on photocatalytic efficiency is not well understood at this time. Furthermore, despite the advantages of noble metal doping, there are several associated drawbacks such as availability, cost and scalability, which may limit their widespread use in photocatalytic degradation systems. This section will address the loading of Ag, Au, Pt, and Pd onto TiO_2 NTAs.

Photogenerated electrons that accumulate on the surface of Ag can rapidly transfer to participate in the pollutant degradation process. Hence, Ag can be used to improve the photocatalytic activity of TiO_2 NTAs.[112] Sun *et al.* doped Ag nanoparticles onto the surface of TiO_2 NTAs through an ultrasound-aided photochemical route.[15] Through changing the concentration of $AgNO_3$ solution, the amount of Ag nanoparticles loaded on TiO_2 NTAs was controlled. Due to the SPR effect, the absorption edges of Ag-loaded TiO_2 NTAs exhibited red-shift and their absorption intensity in the visible light region of 400–650 nm was enhanced. After Ag loading, the photocurrent and photocatalytic degradation rate of the resulting Ag-loaded TiO_2 NTAs photocatalyst under the UV light irradiation were significantly enhanced. The photocatalyst prepared in 0.006 M $AgNO_3$ solution exhibited the largest photocurrent and photocatalytic degradation rate of approximately 1.2 and 3.7 times that of pure TiO_2 NTAs, respectively.[15] Paramasivalm *et al.* also reported the Ag loading on TiO_2 NTAs.[113] It was shown that samples had an improved Acid Orange 7 (AO7) photocatalytic degradation performance under UV light irradiation.

In order to promote the uniform incorporation of small Ag nanoparticles within TiO_2 NTAs and minimize the deposition and clogging at tube entrances, a pulsed current deposition technique was developed (Fig. 5a and b).[21,55] Lai *et al.* reported that Ag-loaded TiO_2 NTAs produced by this method had improved photocurrent and quicker charge transfer rates compared to those prepared by conventional photoreduction methods.[55] As shown in Fig. 5c and d, the enhanced photocurrent and higher incident photon-to-charge carrier efficiency (IPCE) of Ag-loaded TiO_2 NTAs suggested that the photoinduced electron–hole pair recombination was effectively inhibited by the Ag loading into the tubes *via* pulsed current deposition.[20,55] In addition, after Ag loading the samples displayed a weak photoresponse in the wavelength range of 420–500 nm with a maximum at 475 nm (Fig. 5c).[20,55] Ag-loaded TiO_2 NTAs performed better than pure TiO_2 NTAs in photocatalytic and photoelectrocatalytic degradation of MO under the visible and UV light irradiations.[20] He *et al.* decorated fine Ag nanoparticles onto the outer and inner surfaces of TiO_2 NTAs by a wetting-thermal decomposition process.[114] After Ag decoration, samples showed higher photocatalytic capability in the degradation of MB and PCP under UV light irradiation. Tang *et al.* prepared Ag nanoparticles and reduced graphene oxide co-decorated TiO_2 NTAs by combining electrodeposition and photoreduction

Table 2 Methods for preparing metal-ion-decorated TiO_2 NTAs and the corresponding photocatalytic performance

Metal ions	Methods	Light source	Degradation pollutant	Improved photocatalytic efficiency as compared with unmodified ones (%)	Ref.
Fe	Anodization	UV	MB	81.0[a]	52
Fe + α-Fe_2O_3	Ultrasonic-assisted impregnating-calcination	Visible	MB	120.0[a]	18
Zr	Electrodeposition and calcination	UV	RhB	54.7[a]	51
N–Zr	Anodization	UV Visible	RhB	42.6[b] 62.0[b]	111

[a] The number was calculated by $(r_m - r_{unm})/r_{unm}$, where r_m and r_{unm} are apparent rate constants deduced from the slope of linear fitting of $\ln(C_0/C)$ *versus* reaction time using modified TiO_2 NTAs and unmodified TiO_2 NTAs, respectively. C_0 and C are initial and reaction concentrations of the targeted pollutant, respectively. [b] The number was calculated by $(C_{unm} - C_m)/C_{unm}$, where C_m and C_{unm} are the concentrations of the targeted pollutant which was degraded for a certain period of time by using modified TiO_2 NTAs and unmodified TiO_2 NTAs, respectively.

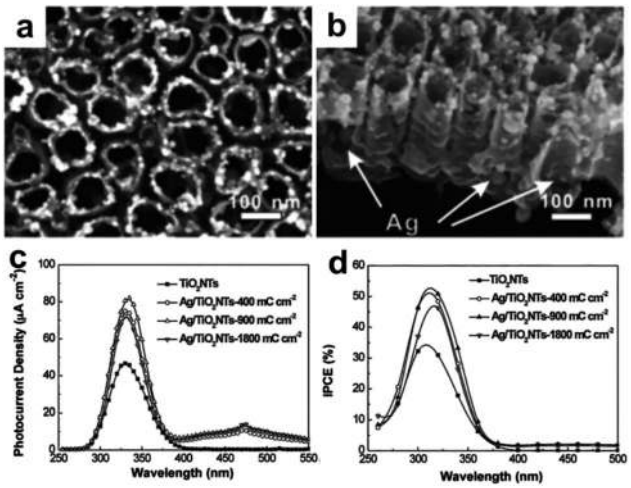

Fig. 5 SEM images of (a) top view and (b) side view of Ag-loaded TiO_2 NTAs obtained by a pulse current deposition technique under the electrodeposition charge density of 900 mC cm^{-2}. (c) Photocurrent densities of TiO_2 NTAs and Ag-loaded TiO_2 NTAs obtained under different electrodeposition charge densities. (d) The corresponding IPCE of TiO_2 NTAs and Ag-loaded TiO_2 NTAs. Adapted with permission from ref. 20, Copyright© 2010 Elsevier.

routes.[115] This kind of ternary catalyst exhibited almost 100% photocatalytic removal efficiency of 2,4-D under simulated solar light irradiation. It presented excellent stability and easy recovery during 10 successive cycles with 1600 min of total irradiation. Clearly, a more systematic understanding of the effect of doping placement within the NTAs, in addition to the identity, is needed. For example, the development of processing techniques which maintain constant atom% incorporations while varying placements of various dopants would provide a better understanding of the per atom performance enhancement.

Au receives much attention because it can strongly interact with visible light and infrared light due to its highly localized SPR properties and photostability.[116,117] Au, as a distinguished electronic conductor, can facilitate rapid transfer of photoinduced electrons on TiO_2 NTAs. Consequently, the recombination of photogenerated charges was restricted and a high quantum yield can be achieved.[56,118] Paramasivalm *et al.* decorated TiO_2 NTAs with 28 nm Au nanoparticles through a sputtering process.[113] After decoration, samples demonstrated improved photocatalytic efficiency under UV light irradiation. Xiao *et al.* developed a self-assembly strategy to prepare well-defined Au-loaded TiO_2 NTAs using a multilayered dendritic dithiolated diethylenetriaminepentaacetic (DTDTPA) ligand as a bridging medium.[19] The monodispersity of Au nanoparticles can be retained after removing DTDTPA by using a post-heating treatment. Au-loaded TiO_2 NTAs exhibited a higher photocatalytic degradation rate of MO and 4-nitrophenol (4-NP) than pure TiO_2 nanoparticles under the UV light irradiation. This is due to Au nanoparticles serving as electron reservoirs and reinforcing the separation of photoexcited charge carriers. Greater attention to the full benefits of gold in photocatalytic degradation is necessary. The inherent complexity of such

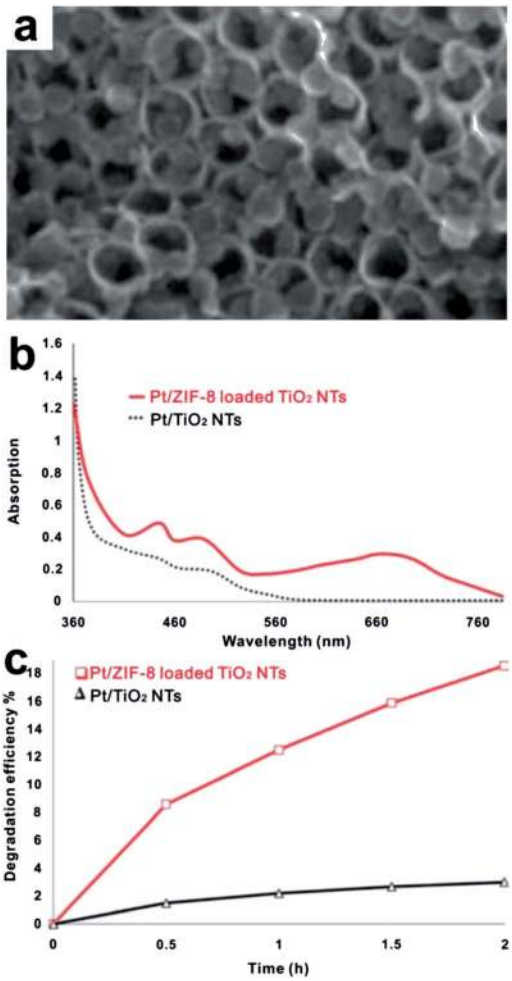

Fig. 6 (a) SEM image of Pt–ZIF-8 loaded TiO_2 NTAs. (b) UV-vis absorption spectra of Pt–ZIF-8 loaded TiO_2 NTAs and Pt-loaded TiO_2 NTAs. (c) Photodegradation of Pt–ZIF-8 loaded TiO_2 NTAs and Pt-loaded TiO_2 NTAs. Adapted with permission from ref. 120, Copyright© 2010 Royal Society of Chemistry.

systems compared to those previously reviewed has limited its development.

The use of Pt-loaded TiO_2 NTAs on photocatalysis has been extensively studied owing to the well-established catalytic properties of the platinum metal in catalytic converters as well as in the splitting of peroxides. The cathodic reduction method was used to load Pt onto TiO_2 nanotubes in chloroplatinic acid.[119] Pt-loaded TiO_2 NTAs with longer tube length had higher photocatalytic activity in degrading MO under UV and visible irradiation. With the decreasing content of anatase, the photocatalytic activity gradually dropped due to the reduction in reactive sites on the surface of Pt-loaded TiO_2.[119] Isimjan *et al.* prepared Pt–zeolitic-imidazolate-framework-8 (Pt–ZIF-8) loaded TiO_2 NTAs (Fig. 6a).[120] Diffuse reflectance UV-vis spectroscopy measurements showed that in comparison to that of Pt-loaded TiO_2 NTAs, Pt–ZIF-8 loaded TiO_2 NTAs had an onset of absorption band significantly red-shifted and were more sensitive to the visible light (Fig. 6b). Under visible light irradiation, the maximum photodegradation efficiency of Pt–ZIF-8

loaded TiO_2 NTAs was 18.6%, reflecting a 510.0% improvement compared to that of Pt loaded TiO_2 NTAs (Fig. 6c). Recently, a facile layer-by-layer self-assembly route was used for the rapid fabrication of well-defined metal–TiO_2 NTA structures (metal = Au, Ag, Pt).[57] Their photocatalytic performance was assessed by the degradation of MO under UV light irradiation. It was found that the photocatalytic performance of metal–TiO_2 NTAs (metal = Au, Ag, Pt) varied with the incorporation of different metal nanoparticles. The kinetic rate constants of photocatalysis followed the order of Pt-loaded TiO_2 NTAs > Au-loaded TiO_2 NTAs > Ag-loaded TiO_2 NTAs > TiO_2 NTAs.

Unlike Ag, Au and Pt, the work function of Pd is lower than the Fermi level of TiO_2.[121,122] This makes the electron transfer from the TiO_2 to Pd energetically favorable, and reduces the photogenerated electron–hole recombination, when an ohmic contact forms at the interface between TiO_2 NTAs and Pd nanoparticles. Recently, Pd nanoparticles of ~10 nm in diameter were uniformly distributed throughout the TiO_2 nanotubular surface using a facile incipient wetness method.[123] After Pd loading, the samples were found to possess excellent photoactivity in the decoloration of methyl red (MR) and MO under UV and visible light irradiation. A Pd loading of around 1.25 wt% proved to be the optimal concentration for the maximum degradation of dyes. Pd-loaded TiO_2 NTAs can be used many times without significant change in activity and structure. Yu *et al.* fabricated Au–Pd-comodified TiO_2 NTAs by a photoreduction method.[124] Malathion was found to be degraded more efficiently using Au–Pd-comodified TiO_2 NTAs than pure TiO_2 NTAs. This was due to a more effective separation of photogenerated electrons and holes and a higher rate of formation of H_2O_2.[124]

SnO_2–Pd-loaded TiO_2 NTA heterostructure photocatalysts were recently synthesized.[125] It was found that the morphology and lattice orientation of TiO_2 NTAs dominated over those of SnO_2–Pd nanoparticles on SnO_2–Pd-loaded TiO_2 NTAs. SnO_2–Pd nanoparticles presented specific orientation growth on TiO_2 NTAs annealed at 450 °C, that is, Pd(111)‖anatase TiO_2(200) and SnO_2(110)‖anatase TiO_2(101), where ‖ refers to Pd and SnO_2 nanoparticles growing parallel to a specific lattice orientation of TiO_2.[125] Meanwhile, when calcinated at 450 °C, the rutile SnO_2 nanoparticles facilitated the conversion of amorphous TiO_2 into rutile phase with the lattice correlation of Pd(111)‖anatase TiO_2(101) and SnO_2(110)‖anatase TiO_2(110).[125]

Clearly, the improved photocatalytic efficiency (under 150% in most cases) of TiO_2 NTA photocatalysts after the noble metal loading remains low and still needs to be increased. The techniques used to craft noble-metal-loaded TiO_2 NTAs and the corresponding enhanced photocatalytic activities are summarized in Table 3. It is important to note that noble metal loading may lead to photoresponse in the visible light region because of the SPR effect. However, few papers discuss how SPR affects the photocatalytic efficiency in detail. Studies, such as simulations and theoretical calculations, focused on how SPR effect works in photocatalysis are still required in order to further understand the SPR effect and provide the guidelines for better noble metal-loading on TiO_2 NTAs.

2.2.3 Heterogeneous structures composed of TiO_2 nanotube arrays and semiconductors. This kind of modification carries three advantages. First, the bandgap of the semiconductor can be easily tuned by changing the particle size. Second, as the semiconductor acts as the sensitizer, photoinduced electrons can directly be transferred from CB of the semiconductor to that of TiO_2. Thus, the visible light absorption of photocatalysts after coupling with semiconductors can be enhanced tremendously. Third, the stability of the semiconductor under light irradiation can be enhanced through changing its crystalline phase to the most stable one, the protective layer coating, *etc.*[126–128] By coupling TiO_2 NTAs with a small bandgap semiconductor, which absorbs visible light and has a more negative CB, a heterogeneously structured photocatalyst can be formed. Under visible light irradiation, photogenerated electrons are prone to be injected from the CB of the

Table 3 Methods for crafting noble-metal-loaded TiO_2 NTAs and the corresponding photocatalytic performance

Noble metals	Methods	Light source	Degradation pollutant	Improved photocatalytic efficiency as compared to unmodified ones (%)	Ref.
Ag	Ultrasound aided photoreduction	UV	MB	270.0[a]	15
	Photoreduction	UV	AO7	140.6[a]	113
	Pulsed current deposition	UV	MO	134.8[a]	20
		Visible		415.6[a]	
Au	Sputtering	UV	AO7	41.7[a]	113
Pt	Direct current electrodeposition	UV	Phenol	138.6[a]	54
	Cathodic reduction	UV	MO	21.5[b]	119
		Visible		235.2[b]	
Pd	Incipient wetness	UV	MR	52.3[b]	123
		Visible		267.8[b]	
Au–Pd	Photoreduction	UV	Malathion	172.0[a]	60

[a] The number was calculated by $(r_m - r_{unm})/r_{unm}$, where r_m and r_{unm} are apparent rate constants deduced from the slope of linear fitting of $\ln(C_0/C)$ *versus* reaction time using modified TiO_2 NTAs and unmodified TiO_2 NTAs, respectively. C_0 and C are initial and reaction concentrations of the targeted pollutant, respectively. [b] The number was calculated by $(C_{unm} - C_m)/C_{unm}$, where C_m and C_{unm} are the concentrations of the targeted pollutant which was degraded for a certain period of time by using modified TiO_2 NTAs and unmodified TiO_2 NTAs, respectively.

small bandgap semiconductor to that of TiO_2. This inhibits the recombination of photogenerated charge carriers which are then transferred to the targeted pollutants. The holes from a small bandgap semiconductor and TiO_2 move to the interface between the target pollutant and the photocatalyst to react with H_2O and OH^- to form $^{\bullet}OH$. This section focuses on the positioning, morphology and size of semiconducting dopants and their resulting effect on the performance of photocatalytic systems. Several common synthesis and processing techniques are also briefly addressed.

Cadmium sulfide (CdS) is a well-understood semiconductor system in traditional electrical applications as well as in nanoscale formulations. This makes it an attractive dopant to be considered in photocatalytic systems. With a bandgap of 2.4 eV, CdS can absorb low energy photons up to 520 nm. The CB of CdS is more negative than that of TiO_2 which facilitates the separation of photoinduced electron–hole pairs. Therefore, coupling TiO_2 with CdS gives more efficient photocatalytic performance by increasing its ability to harvest the visible photons and improving the overall charge separation process.[63] Wang *et al.* developed a constant current electrochemical deposition route to decorate TiO_2 NTAs with CdS nanoparticles. This process used a mixed solution of $CdCl_2$ in dimethyl sulfoxide (DMSO) with saturated elemental sulfur as an electrolyte at 100 °C.[129] In the degradation of RhB, CdS-sensitized TiO_2 NTAs showed the highest photocatalytic degradation rate after 10 min, a 2.6-fold enhancement of photocatalytic activity under visible light irradiation when compared to undoped TiO_2 NTAs.

TiO_2 NTAs can also be loaded with CdS nanoparticles by employing a sonoelectrodeposition approach.[64] The ultrasonication successfully distributed small CdS nanoparticles at a lower temperature (50 °C). In comparison to pure TiO_2 NTAs, CdS-decorated TiO_2 NTAs showed a more than 9-fold enhancement in photocurrent response. Moreover, when compared to CdS-decorated TiO_2 NTAs prepared by plain electrodeposition, CdS-decorated TiO_2 NTAs obtained by sonoelectrodeposition displayed an improved photocurrent and an increased photocurrent response which extended to almost 500 nm.

Xie *et al.* used a sonication-assisted sequential chemical bath deposition (S-CBD) approach to decorate CdS QDs on TiO_2 NTAs.[130] This method prevented CdS QDs from aggregating at the entrance of TiO_2 NTAs, and promoted the deposition of CdS QDs into TiO_2 nanotubes. After CdS decoration, the samples exhibited an enhanced photocurrent generation and photocatalytic efficiency under visible illumination because of a more efficient separation of photogenerated charge carriers. This enhancement was not observed for pure TiO_2 NTAs and CdS-sensitized TiO_2 NTAs fabricated using the same process but without sonication.

Li *et al.* modified TiO_2 NTAs with ultra-fine CdS QDs *via* a cathodic electro-deposition ion-exchange route (CEDIE).[131] Compared to CdS–TiO_2 NTAs prepared by the S-CBD approach,[132] the resulting samples exhibited stronger visible light response, higher photocurrent density, excellent stability, and greatly enhanced PEC activity in degrading MO under visible light irradiation.[131] Chemical liquid deposition was recently utilized to make CdS–S-co-decorated TiO_2 NTAs.[133] It was shown that S^{6+} was doped into the TiO_2 lattice by replacing Ti^{4+}, which decreased the standard reduction potential of CB, and thus enhanced the electron transfer from CdS to TiO_2. Due to the synergy between CdS and S^{6+} as noted above, CdS–S-co-decorated TiO_2 NTAs demonstrated a higher photoactivity than CdS-sensitized TiO_2 NTAs or S-doped TiO_2 NTAs.

Wang *et al.* fabricated Ag and CdS nanoparticle co-sensitized TiO_2 NTAs through a successive ionic layer adsorption and reaction (SILAR) approach.[134] The Ag–CdS-nanoparticle modification expanded the photoresponse range of TiO_2 NTAs from the UV region to 668 nm. The sample prepared by 5-cycle SILAR deposition exhibited the best photocatalytic activity (Fig. 7) and good stability against photocorrosion. Due to the Schottky barrier formed at CdS–Ag junctions,[134] the CdS–Ag-nanoparticle-co-sensitized TiO_2 NTAs showed higher photocatalytic efficiency than pristine TiO_2 NTAs. Recently, Z-scheme type CdS–Ag–TiO_2 NTAs were obtained by using a pulsed current deposition method (Fig. 8a).[21] Fig. 8b shows that the Ag–CdS nanoparticles were composed of Ag cores and CdS shells. Compared with the two-component (*e.g.*, Ag-loaded TiO_2 NTAs or CdS-decorated TiO_2 NTAs) and single-component (*i.e.*, pure TiO_2 NTAs) systems, three-component (*e.g.*, CdS–Ag–TiO_2 NTAs) systems exhibited enhanced photoelectrochemical and

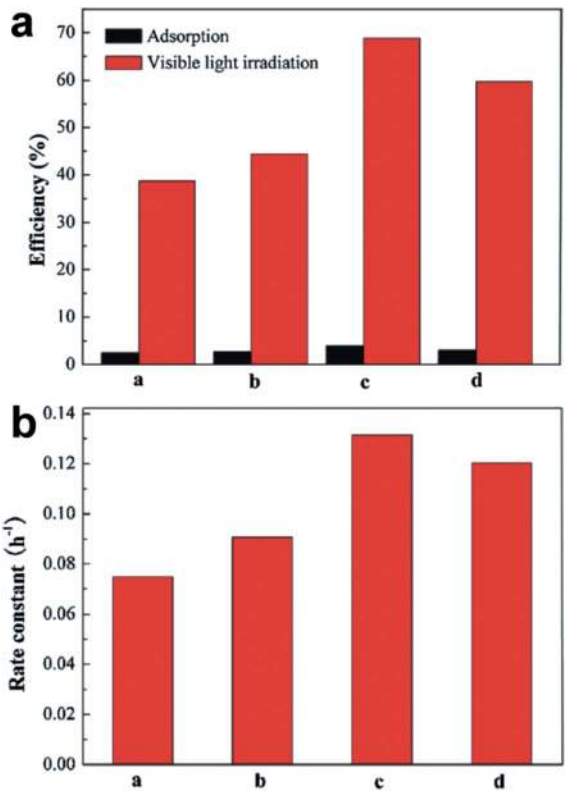

Fig. 7 (a) The adsorption and degradation efficiencies (black: adsorption and red: degradation) and (b) degradation rate constants of MO for different samples: (a) CdS-coupled TiO_2 NTAs and (b–d) Ag–CdS-co-sensitized TiO_2 NTAs prepared by (b) 3-cycle, (c) 5-cycle and (d) 7-cycle SILAR deposition, respectively. Adapted with permission from ref. 134, Copyright© 2010 Elsevier.

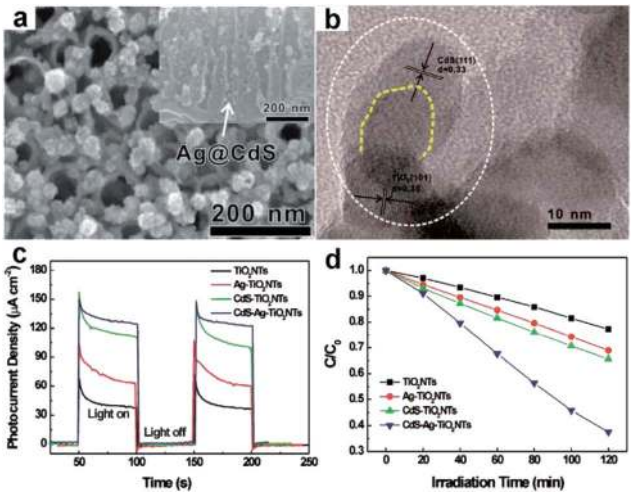

Fig. 8 (a) SEM image of CdS–Ag-co-decorated TiO_2 NTAs. (b) High resolution TEM of CdS–Ag-co-decorated TiO_2 NTAs. (c) Photocurrent response and (d) photocatalytic degradation of MB under UV light irradiation on pure TiO_2 NTAs, Ag-loaded TiO_2 NTAs, CdS-decorated TiO_2 NTAs and CdS–Ag-co-decorated TiO_2 NTAs, respectively. Adapted with permission from ref. 21, Copyright© 2011 Elsevier.

photocatalytic activities (Fig. 8c and d). This is because the photogenerated electrons transferred through a well-defined route (*i.e.*, CdS → Ag → TiO_2) in the three-component system.

It is important to note that CdS can be easily photocorroded.[128] To solve this problem, CdS–ZnO-co-sensitized TiO_2 NTAs were fabricated by filling one-dimensional TiO_2 NTAs with CdS nanoparticles, followed by coating ZnO nanorods on CdS-sensitized TiO_2 NTAs as a protective layer.[128] The empty-bottle-with-a-lid structure protected CdS nanoparticles from photocorrosion, and consequently the photocatalyst stability was improved. ZnO played an important role in both protecting CdS nanoparticles from photocorrosion and promoting the separation of photoexcited charge carriers in the co-sensitized photocatalyst based on the proper band alignment. The photocatalyst had a broad-wave photoresponse and high photocatalytic and photoelectrocatalytic activity under UV and visible light irradiation. The addition of Na_2S into organic pollutants can also contribute to the stability of the CdS-sensitized photocatalyst.[135] CdS–TiO_2-nanoparticle-co-decorated TiO_2 NTAs were recently fabricated *via* the SILAR approach. It was found that a small amount of Na_2S (0.02 M) improved the stability of the CdS-driven photocatalytic process by permitting better separation of photogenerated electron–hole pairs and improving the MO photodegradation.[135]

Since sulfur has a negative impact on the environment, another environmentally friendly element, selenium (Se), has been found for replacing sulfur in many applications. Like sulfur, Se belongs to the oxygen group (chalcogens). The bandgap of CdSe is 1.8 eV, which is much lower than that of CdS. Consequently, CdSe has garnered much attention. Recently, the inner and outer surfaces of TiO_2 NTAs were decorated by CdSe nanoparticles through a direct current electrochemical technique.[136] The resulting samples showed high photoresponse due to the narrow bandgap of CdSe and exhibited immediate and steady photocurrent under monochromatic visible light irradiation. Under 550 nm green light illumination, CdSe-coupled TiO_2 NTAs demonstrated higher photocatalytic activity in degrading anthracene-9-carboxylic acid (9-AnCOOH) when compared to uncoupled TiO_2 NTAs. However, CdSe is easily photocorroded.[137] In order to prevent photocorrosion of CdSe, Ouyang *et al.* fabricated CdSe–TiO_2 sensitized TiO_2 NTAs *via* an ultrasonic-assisted cyclic voltammetry electrochemical deposition process and wrapped as-prepared samples by a thin TiO_2 layer using the $TiCl_4$ hydrolysis treatment.[138] It was shown that CdSe nanoparticles were prone to disperse in anodized TiO_2 NTAs, and the CdSe coupling increased with an increase in voltammetry cycles. The resulting samples possessed visible light photoelectrocatalytic activity in the degradation of glucose.

Continuing down the chalcogen group, Te is found. CdTe has a bandgap of 1.6 eV, which is narrower than CdS and CdSe. Thus, CdTe can utilize solar light more efficiently than the other two. Feng *et al.* used a pulsed electrodeposition technique to obtain CdTe-coupled TiO_2 NTAs.[139] CdTe-sensitized TiO_2 NTAs remained stable in the photocatalytic degradation of *p*-nitrophenol (PNP) after ten repeated runs which can be attributed to a highly stable physical construction and high anti-photocorrosion property. Under visible light irradiation, CdTe-sensitized TiO_2 NTAs exhibited a much higher degradation rate (0.0312 min^{-1}) than unmodified TiO_2 NTAs (0.0071 min^{-1}). Instability and toxicity are two main problems in CdX (X = S, Se, Te)-coupled TiO_2 NTA photocatalysts. More efforts should be made to address this issue from the standpoint of safety and minimization of their use.

Cu_2O, a p-type semiconductor with a bandgap of 2.17 eV and a more negative CB than in TiO_2, has attracted much attention. It has been shown to be a promising photocatalyst in organic pollutant degradation under visible illumination.[140] Cu_2O acts as a sensitizer and facilitates electron transfer to the CB of TiO_2, thereby effectively separating photogenerated electron–hole pairs.[17] Cu_2O can also effectively absorb oxygen,[141] which reacts rapidly with the photoinduced electrons, and the recombination of charge carriers is thus reduced. As a consequence, Cu_2O coupling improves the photocatalytic efficiency in a way unlike other semiconductor doped NTA systems.

Hou *et al.* fabricated Cu_2O-coupled TiO_2 NTAs using a photoreduction method.[142] The hybrid photocatalyst exhibited a higher efficiency than the unmodified TiO_2 in the photocatalytic and photoelectrocatalytic decomposition of PNP. Cu_2O nanoparticles were shown to enhance the efficiency of photo-harvesting and reduce the recombination of electron–hole pairs by transferring electrons to the CB of TiO_2. TiO_2 NTAs can also be coupled with Cu_2O nanoparticles *via* an electrodeposition process using $CuSO_4$ as the Cu source.[143,144] The photocatalytic activity of TiO_2 NTAs after modification was dramatically enhanced by the modification of octahedral Cu_2O. This is due to the exposure of a large area of {111} facets of octahedral Cu_2O, which improved the adsorption and photocatalytic activity.[143]

The content of polyhedral crystalline Cu_2O can be controlled by varying the electrodeposition charges.[145] Under visible light

irradiation, the photocatalytic AO7 decolorization efficiency of the samples obtained with a deposition charge of 500 mC was about 18 times that of unmodified TiO_2 NTAs. Wang *et al.* crafted Cu_2O-modified TiO_2 NTAs p–n heterojunction photoelectrodes by capitalizing on the S-CBD technique.[17] The photocatalysts with a small amount of Cu_2O nanoparticles decorated on TiO_2 NTAs (obtained from the ultrasonication deposition of Cu_2O nanoparticles with its most stable crystalline phase (111) for 4 min, Fig. 9a) exhibited the largest photocurrent (Fig. 9b) and the highest photocatalytic activity under visible light irradiation (Fig. 9c). Under an applied 0.5 V bias potential, Cu_2O-modified TiO_2 NTAs were found to possess high photoelectrocatalytic efficiency due to a synergistic effect of electricity and visible light (Fig. 9d). However, oxidation of Cu_2O to CuO occurs readily in solution and under light irradiation. The chemical stability of Cu_2O needs to be improved to meet the requirement of large-scale industrial applications.

Similar to Cu, Fe is abundant on the earth. Fe_2O_3 remains much more stable than Cu_2O in neutral and alkaline solution. With a bandgap of 2.2 eV, Fe_2O_3 is well suited for capturing a significant portion of the solar spectrum with a maximum theoretical photoconversion efficiency of 12.9%.[146] γ-Fe_2O_3-coupled TiO_2 NTAs were fabricated using an ultrasonic-assisted immersion technique.[147] The study demonstrated that γ-Fe_2O_3-coupled TiO_2 NTAs not only maintained the photocatalytic performance of pristine TiO_2 NTAs, but also displayed higher photocatalytic performance with a relatively small amount of γ-Fe_2O_3 nanoparticle decoration. The electrochemical impedance and Mott–Schottky measurements confirmed the improvement of the interfacial electron transfer kinetics for γ-Fe_2O_3-decorated TiO_2 NTA photocatalysts (Fig. 10). This enhanced charge transfer between semiconductors (*i.e.*, γ-Fe_2O_3 and TiO_2) led to improved photocatalytic efficiency in the degradation of MO and the transformation of surface properties of γ-Fe_2O_3-decorated TiO_2 NTAs from initially superhydrophilic to less hydrophilic. Notably, it has been reported that α-Fe_2O_3 is the most stable form of iron oxide and commonly found in rocks and sediments on the earth.[148] Cong *et al.* deposited α-Fe_2O_3 on TiO_2 NTAs by an electrochemical deposition process.[149] The resulting α-Fe_2O_3-modified TiO_2 NTAs were more effective than α-Fe_2O_3 nanoparticles and TiO_2 NTAs alone in the photoelectro-Fenton degradation of phenol, which was almost completely removed with α-Fe_2O_3-modified TiO_2 NTAs after 60 min.[149] α-Fe_2O_3-modified TiO_2 NTAs also possessed good stability in photoelectro-Fenton reactions. As Fe_2O_3 is an alkaline oxide, it is not stable in acid solution and thus is restricted to degradation in neutral and alkaline solution.

Similar to Fe_2O_3, NiO is also stable in neutral and alkaline solution. Many studies have focused on NiO. p-Type NiO species can act as hole collectors.[150] When TiO_2 NTAs are coupled with NiO, the recombination rate of photo-generated charge carriers is greatly reduced.[151,152] Shrestha *et al.* prepared NiO-sensitized TiO_2 NTAs by the chemical bath deposition (CBD) technique.[152] In comparison to N-doped TiO_2 NTAs, NiO-sensitized samples

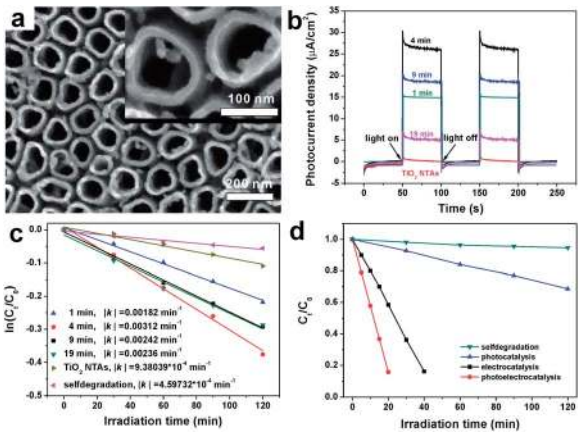

Fig. 9 (a) SEM image of Cu_2O-modified TiO_2 NTAs. (b) Photoresponse and (c) photocatalytic degradation rates of RhB for TiO_2 NTAs and Cu_2O-modified TiO_2 NTAs prepared for different times. (d) Comparisons of photocatalytic, electrocatalytic, and photoelectrocatalytic degradation of RhB for Cu_2O-modified TiO_2 NTAs prepared for 4 min. All the above results were obtained under visible light irradiation. Adapted with permission from ref. 17, Copyright© 2013 Royal Society of Chemistry.

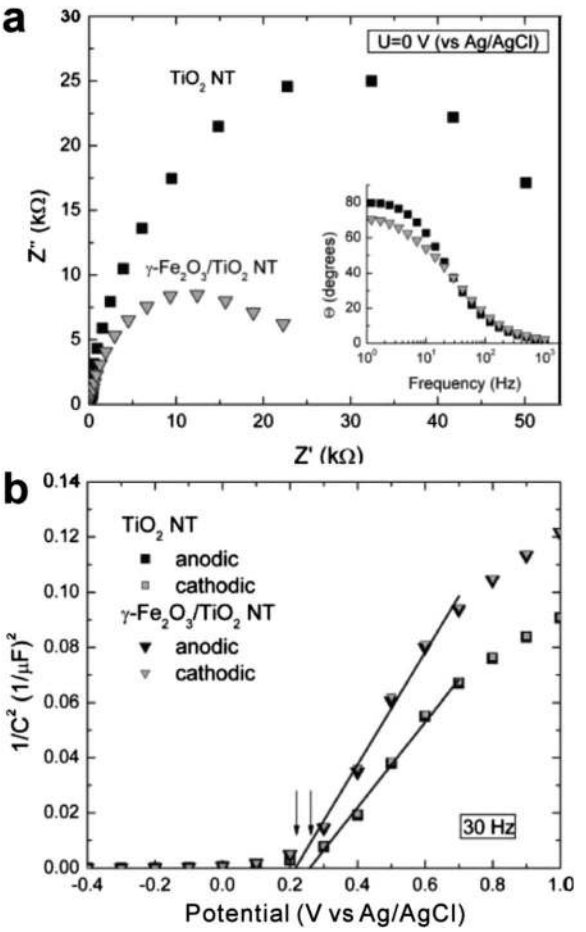

Fig. 10 (a) EIS Nyquist plots and (b) Mott–Schottky plots for γ-Fe_2O_3-coupled TiO_2 NTAs (5 mg mL^{-1} γ-Fe_2O_3) and pure TiO_2 NTAs. The inset in (a) shows the corresponding variation of the phase angle as a function of frequency (Bode plot) for the two samples. Adapted with permission from ref. 147, Copyright© 2009 American Chemical Society.

showed higher visible light photoresponse and photocatalytic activity.[152] NiO nanoparticles were also successfully deposited onto TiO_2 nanotubes *via* an incipient wet impregnation method.[153] It was found that the majority of Ni existed as NiO and the remaining Ni was incorporated into the TiO_2 lattice. Under different amounts of NiO decoration, the samples demonstrated higher degradation efficiency than pure TiO_2 NTAs.

The degradation rate of MB was found to be independent of NiO concentration as TiO_2 NTAs with different amounts of NiO decoration exhibited almost the same absorption band.[153] Further study on photocatalytic mechanism is still needed in order to have a better understanding as to why the concentration of NiO modification does not appear to affect photocatalytic performance of NiO-coupling TiO_2 NTAs. Similar to Fe_2O_3, NiO is easily degraded in acid solution. Hence, stability improvements in NiO and related dopant strategies remain a big problem to be addressed.

Due to its improved stability in different solutions compared with Fe_2O_3 and NiO, ZnO has received great interest. With almost the same wide bandgap (3.2 eV) as TiO_2, ZnO plays an important role in electron transport when combined with TiO_2. Photoexcited electrons would transfer from the CB of ZnO to that of TiO_2, and meanwhile holes would transfer from the VB of TiO_2 to that of ZnO. These quick transfer processes can thus decrease the recombination rate of charge carriers.[154,155]

ZnO nanorods can serve as channels for photogenerated holes, efficiently promoting the separation of electron–hole pairs. ZnO nanorods were recently crafted on the top of TiO_2 NTAs by a seed-induced hydrothermal reaction[156] and cathodic electrodeposition.[157]

ZnO-coupled TiO_2 NTAs with a ZnO content of 0.65 mg cm^{-2} demonstrated higher photocatalytic activity than pure TiO_2 NTAs or ZnO nanorods in the photoelectric degradation of bisphenol A (BPA).[156] Yang *et al.*[158] fabricated ZnO-modified TiO_2 NTAs by the room-temperature deposition of ZnO plasma using the filtered cathodic-vacuum-arc technique (Fig. 11a). Compared with pure ZnO nanorods and TiO_2 NTAs, the samples after ZnO modification showed better photocatalytic performance in the decomposition of humic acid (HA) (Fig. 11c).[158] This is attributed to the nanotubular geometry that provided metal oxides with large surface area to the surroundings and an improvement in charge separation of photogenerated charge carriers within heterojunction nanostructures.[158,159] Single crystal ZnO nanorods can also be deposited on TiO_2 NTAs to increase total surface area of photocatalysts. When acting as supporting platforms for Ag nanoparticle deposition, ZnO nanorods deposition renders photocatalysts to possess more Ag nanoparticles, and thus enhances the photocatalytic activity.[160] It was found that ZnO nanorods were nucleated on TiO_2 nanotubes and grew along the [002] direction following the structural correlation ZnO (100)||TiO_2(103). The Ag–ZnO-sensitized TiO_2 NTAs multijunction heterostructured photocatalyst displayed superior photocatalytic activity when compared to pristine TiO_2 NTAs.[160] Due to a large bandgap of 3.2 eV, ZnO can only be excited by UV light. Consequently, it has found limited use. Tuning the size of ZnO nanoparticles will enable modulation of the bandgap.

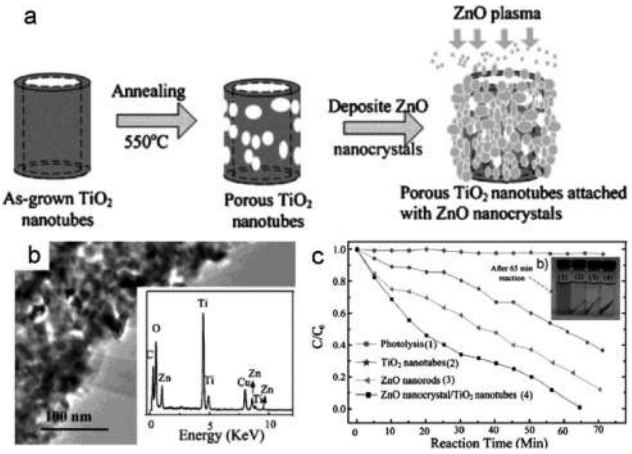

Fig. 11 (a) Fabrication process of ZnO-modified TiO_2 NTAs. (b) TEM image of ZnO-modified TiO_2 NTAs. The inset presents the EDX spectra of the sample. (c) Photocatalytic decomposition rates of HA using TiO_2 NTAs, ZnO nanorods and ZnO-modified TiO_2 NTAs. (1) Reference HA solution, (2) TiO_2 NTAs, (3) ZnO nanorods, and (4) ZnO-modified TiO_2 NTAs. The insets show the photographs of HA after 65 min photocatalytic decomposition by the four samples noted above. Adapted with permission from ref. 158, Copyright© 2009 Wiley-VCH.

Besides the large bandgap of ZnO, SnO_2 with an even larger bandgap (3.7 eV) is also used to modify TiO_2 NTAs. Different from other semiconductor coupling mechanisms, TiO_2 acts as the sensitizer, while SnO_2 serves as the electron collector. Macroporous SnO_2 was assembled by a liquid crystal soft template method in the presence of TiO_2 NTAs to yield SnO_2-coupled TiO_2 NTAs.[161] The bandgap of the sample after SnO_2 coupling became 2.93 eV because of the bandgap matching between SnO_2 and TiO_2.[162] Such a hybrid photocatalyst also had smaller resistance and smaller impedance between the catalyst and the electrolyte, lower activation energy of electrochemical reaction, and higher removal rate of 2,4-D than the TiO_2 NTA photocatalyst.

The large bandgap of SnO_2 may, however, inhibit the utility of this system in photocatalysis despite the improved stability and the different fundamental operating mechanism. Hence, it is desirable to lower the bandgap of this system while maintaining said advantages. This can be accomplished through doping with other metals. The bandgap of SnO_2 can be reduced when metals, such as antimony (Sb), are doped into the lattice of SnO_2.[163] Sb^{5+} can replace the site of Sn^{4+} in SnO_2, generating an extra electron, and thus increasing the conductivity of SnO_2.[163] Li *et al.* deposited Sb-doped SnO_2 nanoparticles into TiO_2 NTAs.[164] Intermixing of SnO_2 and TiO_2 lattices led to strong combination between TiO_2 and Sb-doped SnO_2. A sieve-like macroporous Sb-doped SnO_2 film was decorated on TiO_2 NTAs using a block copolymer soft-template technique.[165] The decomposition of benzoic acid (BA) and PNP during the PEC process was found to be higher than the sum of that in the individual photocatalytic (PC) and electrocatalytic (EC) processes. Cooperative effects of electrocatalysis and photocatalysis were recognized in the Sb–SnO_2-co-sensitized TiO_2 NTAs.[164,165] It is intriguing to find that after TiO_2 NTAs are

coupled with SnO_2, which possesses a larger bandgap, the bandgap of the sample becomes narrower than both TiO_2 and SnO_2. However, the bandgap is still so wide that photocatalysts cannot effectively utilize solar light. Clearly, the trend that emerges from the previous material investigations is that the nanoscale construction of dopants of specific and controllable sizes enables readily available and inexpensive materials to be incorporated into functional dopants in improved photocatalysts.

With a narrower bandgap (1.52 eV) compared with ZnO and SnO_2, $CuInS_2$ possesses a direct bandgap well-matched to the solar spectrum as well as a high absorption coefficient.[166] Recently, $CuInS_2$ nanoparticles were deposited onto TiO_2 NTAs by using pulsed electrodeposition to obtain p–n $CuInS_2$-sensitized TiO_2 NTAs heterojunction photocatalysts. These structures exhibited increased photocurrent density and enhanced photocatalytic and photoelectrocatalytic activity in the decolorization of 2,4-D (Fig. 12).[167] The enhanced photodegradation efficiency is attributed to the improved visible-light absorption and decreased photogenerated charge carrier recombination. However, fabrication of $CuInS_2$ usually requires expensive starting materials (indium precursors), which limits its large-scale application in such devices.

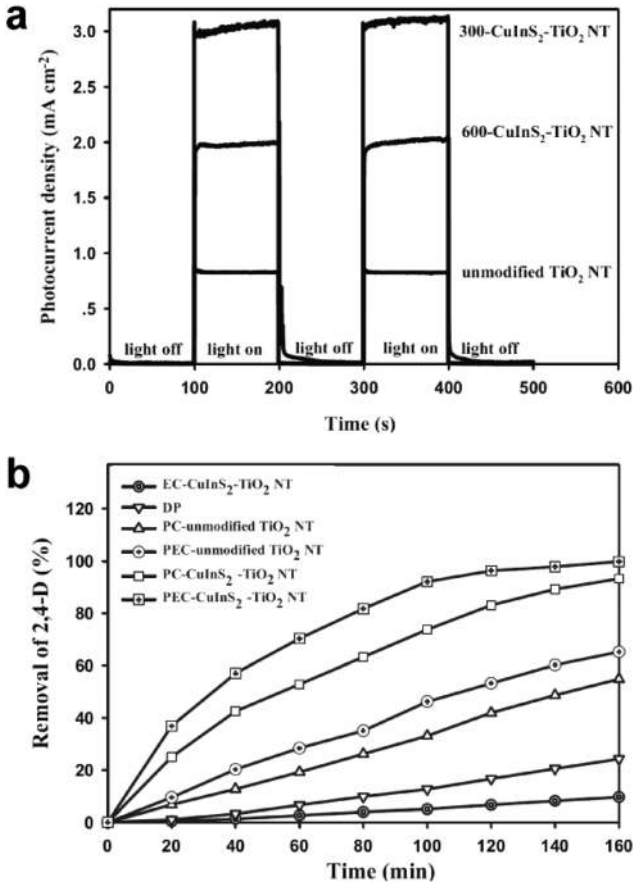

Fig. 12 (a) Photocurrent responses of pure TiO_2 NTAs and $CuInS_2$-modified TiO_2 NTAs under 300 and 600 pulse sequences in 0.05 M Na_2SO_4 solution. (b) Electrochemical (EC), direct photolytic (DP), photocatalytic (PC) and photoelectrocatalytic (PEC) degradation of 2,4-D using TiO_2 NTAs and $CuInS_2$-modified TiO_2 NTAs under 300 pulse sequences. Adapted with permission from ref. 167, Copyright© 2011 Elsevier.

As a more promising material with low cost, $ZnFe_2O_4$ has received increasing attention due to its better stability and visible light activity in comparison with other inorganic semiconductors (*e.g.* NiO, Fe_2O_3 *etc.*). $ZnFe_2O_4$ is a spinel-type (AB_2O_4) semiconductor with a relatively narrow bandgap (*ca.* 1.9 eV). Nanometer-sized $ZnFe_2O_4$-modified TiO_2 NTAs are potentially useful solar energy materials for photocatalysis in the decolorization of organic pollutants due to their advantageous visible light response and photo-corrosion resistance.[168–173]

Recently, $ZnFe_2O_4$-modified TiO_2 NTAs were prepared by cathodic electrodeposition and hydrothermal methods.[62,174,175] Through the cathodic electrodeposition method, $ZnFe_2O_4$ nanoparticles were dispersed inside the TiO_2 tubes and their aggregation at tube entrances was minimized. The resulting photocatalysts displayed strong photoresponse and higher photocurrent density in the visible region.[174]

Compared to unmodified TiO_2 NTAs, $ZnFe_2O_4$-sensitized TiO_2 NTAs showed an improved PEC efficiency in the decomposition of PNP. As evidenced in electrochemical impedance spectroscopy (EIS) measurements (Fig. 13), Wang *et al.* found that the deposition of $ZnFe_2O_4$ nanoparticles can reduce the charge transfer resistance and enhance the electron mobility. This effectively inhibits the recombination and promotes the transfer of photo-induced charge carriers.[175] More studies should be focused on modulating the grain size of $ZnFe_2O_4$ nanoparticles to narrow the bandgap and get better utilization of the solar light spectrum.

We note that relatively simple crystalline dopants have been discussed above. However, dopants of more complicated structure and morphology are also of interest. In the following, allotropes and combinations related to carbon-based semiconductors are reviewed.

Some special semiconductors composed of carbon have attracted great interest.[176–178] Recently, C_{60}-modified TiO_2 NTAs were formed by electrodeposition.[44] The highest PEC activity of C_{60}-modified TiO_2 NTAs was achieved at the bias potential of 4.0 V in degrading MB under a germicidal lamp ($\lambda = 254$ nm). The high PEC activity originated from the synergy between C_{60} and TiO_2, namely, facilitating the charge separation, improving the charge distribution in the electrical double layer, and decreasing the Helmholtz impedances and depletion layers.

In addition, graphene films can be dispersed onto TiO_2 NTAs by electrodepositing graphene from graphene oxide (GO) with different deposition cycle numbers. The resulting graphene–TiO_2 NTAs exhibited a considerably increased degradation rate of anthracene-9-carboxylic acid (9-AnCOOH) as compared to pure TiO_2 NTAs.[178] 26-Cycle electrodeposited graphene-modified TiO_2 NTAs displayed the highest removal rate. This is because the largest interfacial area was formed between graphene and TiO_2 NTAs at the 26-cycle graphene electrodeposition, and further graphene loading hindered the light transmittance to TiO_2 NTAs due to thicker graphene layers.[178] As GO is environmental friendly and possess unique physicochemical properties, it has been widely studied in recent years.[179,180] A novel hybrid material composed of a GO network

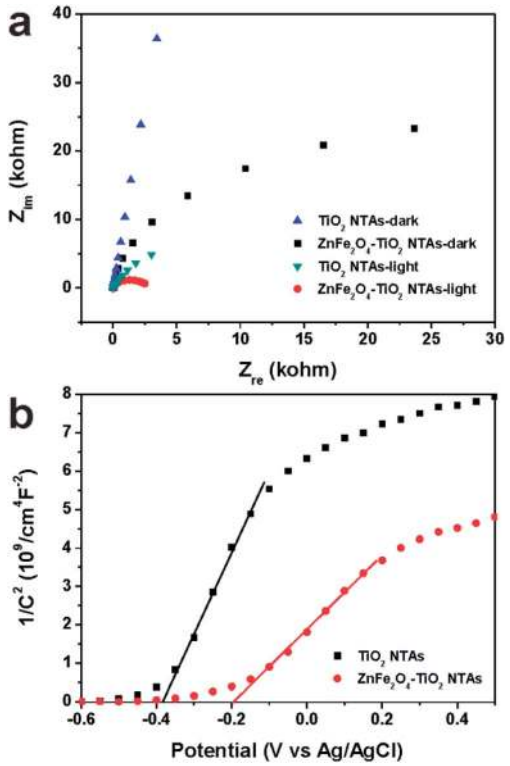

Fig. 13 (a) Nyquist plots of the electrochemical impedance spectra (Z_{re} *vs.* Z_{im}) and (b) Mott–Schottky plots for TiO_2 NTAs and $ZnFe_2O_4$-coupled TiO_2 NTAs, respectively. Adapted with permission from ref. 175, Copyright© 2013 Royal Society of Chemistry.

on the surface of TiO_2 NTAs has been developed.[181] The photoconversion efficiency of GO-modified TiO_2 NTAs was about 15 times higher than that of a pure unmodified system. Due to the sensitizing effect of GO, GO-modified TiO_2 NTAs had a relatively high photocatalytic degradation rate under visible light irradiation. For the first time, Pan *et al.* reported a controllable electrophoretic method for crafting a graphene-quantum-dot (GQD) sensitized TiO_2 NTAs photocatalyst (Fig. 14a–c).[182] This photocatalyst showed excellent PEC activity under visible light irradiation (Fig. 14d) and remained stable over many cycles (400 min/4 cycles). The photocatalytic degradation mechanism can be rationalized as follows. The lowest occupied molecular orbital (LUMO) energy level of GQDs is higher than the bottom of the TiO_2 CB, suggesting that electrons can transfer from GQDs to TiO_2 when GQDs are excited by the visible light. The effective separation of photoexcited electrons is thus realized, leading to enhanced photocatalytic performance. However, the optical bandgap of GQDs (2.90 eV) remains relatively wide, thereby limiting the visible light sensitization of TiO_2 NTAs. In order to maximize the visible-light harvesting, further reduction of the bandgap *via* tuning the size and edge effects of GQDs is necessary.

The methods used to prepare semicondutor-coupled TiO_2 NTAs and the corresponding photocatalytic performance are summarized in Table 4. The photocatalytic performance of semiconductor-decorated TiO_2 NTAs typically increases by more than 150% when compared to pristine TiO_2 NTAs (Table 4).

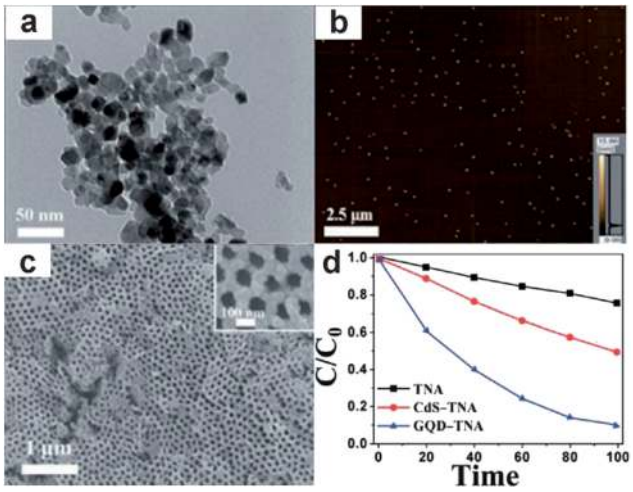

Fig. 14 (a) TEM image and (b) AFM image of GQDs. (c) SEM image of GOD-sensitized TiO_2 NTAs. (d) The PEC degradation rate for different photocatalysts. Adapted with permission from ref. 182, Copyright© 2013 Royal Society of Chemistry.

More efforts should be made in order to enhance the stability of semiconductors. In addition, the effects of the grain size of semiconductor materials on photocatalyst performance should be further investigated. Furthermore, despite the performance enhancements reported here, it is difficult to make useful comparisons between different systems using commonly available metrics. Hence, more standardized and universal methods of gauging efficiency are essential to make useful comparisons between different modifying classes of TiO_2 NTAs. The performance enhancements detailed herein are only useful for assessing relative enhancement of NTAs within each class.

3. Concluding remarks and outlook

Semiconductor TiO_2 NTAs have emerged as promising photocatalyst nanomaterials for utilizing solar energy in the photodegradation of environmentally-relevant organic pollutants and toxic compounds. They possess high surface-to-volume ratios and unique nanotube array structures that facilitate efficient charge transfer. This Review briefly introduces the mechanisms of photocatalysis, and then concentrates on three strategies (*i.e.*, modifying TiO_2 NTAs with non-metals, metals, and semiconductors) that are widely used to yield high efficiency TiO_2 NTA photocatalysts. These judiciously modified TiO_2 NTAs exhibit improved UV and visible light absorptions, and thus harvest an increased portion of the solar spectrum. Moreover, the recombination of photogenerated electron–hole pairs is largely reduced or inhibited. Among the three strategies, semiconductor doping represents the most promising route to enhanced photocatalytic efficiency due to the large availability and controllability of energy levels within semiconductor species.

Despite the significant advantages of these three strategies to produce high performance photocatalysts over the unmodified TiO_2 NTAs, several issues remain to be addressed. First, it is

Table 4 Methods for producing semicondutor-coupled TiO_2 NTAs and the corresponding photocatalytic performance

Semiconductors	Methods	Light source	Degradation pollutant	Improved photocatalytic efficiency as compared to unmodified ones (%)	Ref.
CdS	Constant current electrochemical deposition,	Visible	RhB	255.2[a]	129
	SILAR	Visible	MO	362.5[a]	135
CdTe	Pulsed electrodeposition	Visible	PNP	339.4[a]	139
Cu_2O	Photoreduction,	UV	PNP	492.5[b]	142
	Electrodepositon,	Visible	AO7	170.0[b]	144
	Ultrasonic-assisted S-CBD	Visible	RhB	232.6[a]	17
Fe_2O_3	Ultraonic-assisted immersing	UV	MO	30[a]	147
ZnO	Electrodeposition	UV	MO	72[b]	157
$ZnFe_2O_4$	Electrodeposition	Visible	PNP	165.4[b]	174
$CuInS_2$	Pulsed electrodeposition	Visible	2,4-D	230[a]	167
NiO	Incipient wet impregnation	Solar light	MB	100[a]	153
SnO_2	Sol–gel in a vacuum	UV	BA	176.9[a]	164
	Liquid crystal soft template	UV	2,4-D	158.3[a]	161
C (graphene)	*In situ* electrochemical deposition	Simulated solar light	9-AnCOOH	113.0[b]	178
GOD	Electrophoresis deposition	Visible	MB	756.6[b]	182

[a] The number was calculated by $(r_m - r_{unm})/r_{unm}$, where r_m and r_{unm} are apparent rate constants deduced from the slope of linear fitting of $\ln(C_0/C)$ *versus* reaction time using modified TiO_2 NTAs and unmodified TiO_2 NTAs, respectively. C_0 and C are initial and reaction concentrations of the targeted pollutant, respectively. [b] The number was calculated by $(C_{unm} - C_m)/C_{unm}$, where C_m and C_{unm} are the concentrations of the targeted pollutant which was degraded for a certain period of time by using modified TiO_2 NTAs and unmodified TiO_2 NTAs, respectively.

challenging to compare the photocatalytic activities of different photocatalysts in the literature. Consolidated measurement standards, such as fixed intensity of incident light and concentration of targeted organic dyes in photocatalysis, need to be implemented.

Second, when coupling with semiconductors that absorb the visible photons and degrading organic dyes under the visible light irradiation, TiO_2 NTAs simply act to transfer electrons and suppress the recombination of photoinduced charge carriers without actually contributing to charge carrier generation. Therefore, future research efforts may be directed to fabricate NTAs of different chemical compositions with good chemical and physical stabilities to absorb a broader solar spectrum and take advantage of the high surface area of NTAs and the directed charge transfer pathways enabled by NTAs. Third, most research focuses on capturing visible light, while paying less attention to the infrared radiation which accounts for a large portion of the solar spectrum. Obviously, materials that can efficiently harvest infrared photons are highly desirable for coupling with TiO_2 NTAs. For example, new generation fluorophores, also termed up-conversion nanoparticles, can absorb low energy infrared light and convert it into high energy radiation including visible and UV lights. Four, most studied photocatalysts are usually crystalline samples instead of amorphous ones. Intensive studies on amorphous photocatalysts are also needed. Because of disordered electronic states between the bandgaps, amorphous photocatalysts might have a broader light absorption region than crystalline counterparts. In addition, the usable life of modified TiO_2 NTAs and photocatalytic processes remain to be increased. Having the ability to repair themselves, self-healing materials are an emerging area to be considered.[183] Clearly, modification techniques as well as rational designs of new NTAs other than TiO_2 are still a long way down the road for actual photocatalyst production and should remain an active area of exploration.

Looking forward into the future of this exciting and diverse field, it is important to keep several questions in mind as well. First, there are practical limits to what constitutes improved efficiency, meaning that a compromise must exist between material processing, cost, and performance and that being more efficient isn't always practical or even necessary. Second, the large number of systems presented here represents an invaluable aspect of photocatalysis research. This Review only presents a few of the types of pollutants that can be degraded by hybrid TiO_2 NTAs. Thus the existence of many types of pollutants, currently present and yet to be realized, may require myriad photocatalysts to be invented even beyond those developed thus far. With these two factors in mind, the future of the field of hybrid TiO_2-based NTAs looks wide open and rich with areas of unrealized potential and important problems to be addressed.

Acknowledgements

We gratefully acknowledge the support from the Georgia Institute of Technology and Minjiang Scholar Program at Xiamen University (ZL), and the National Natural Science Foundation of China (51072170 and 21021002) and the National Basic Research Program of China (2012CB932900) (CL). M.W. acknowledges the financial support from the Chinese Scholarship Council.

Notes and references

1 A. Genter, *Sewage Works J.*, 1934, **6**, 689–720.

2 M. Zhu, L. Lee, H. Wang and Z. Wang, *J. Hazard. Mater.*, 2007, **149**, 735–741.
3 J. Leentvaar and M. Rebhun, *Water Res.*, 1982, **16**, 655–662.
4 L. Sun, E. Perdue and J. McCarthy, *Water Res.*, 1995, **29**, 1471–1477.
5 R. Asahi, T. Morikawa, T. Ohwaki, K. Aoki and Y. Taga, *Science*, 2001, **293**, 269–271.
6 A. Fujishima, X. T. Zhang and D. A. Tryk, *Surf. Sci. Rep.*, 2008, **63**, 515–582.
7 I. K. Konstantinou and T. A. Albanis, *Appl. Catal., B*, 2004, **49**, 1–14.
8 J. C. Yu, J. G. Yu, W. K. Ho, Z. T. Jiang and L. Z. Zhang, *Chem. Mater.*, 2002, **14**, 3808–3816.
9 J. L. Gole, J. D. Stout, C. Burda, Y. B. Lou and X. B. Chen, *J. Phys. Chem. B*, 2004, **108**, 1230–1240.
10 M. Iwase, K. Yamada, T. Kurisaki, O. O. Prieto-Mahaney, B. Ohtani and H. Wakita, *Appl. Catal., B*, 2013, **132**, 39–44.
11 Y. K. Lai, L. Sun, Y. C. Chen, H. F. Zhuang, C. J. Lin and J. W. Chin, *J. Electrochem. Soc.*, 2006, **153**, D123–D127.
12 D. Li, H. Haneda, S. Hishita and N. Ohashi, *Chem. Mater.*, 2005, **17**, 2596–2602.
13 A. L. Linsebigler, G. Lu and J. T. Yates Jr, *Chem. Rev.*, 1995, **95**, 735–758.
14 S. Sato, R. Nakamura and S. Abe, *Appl. Catal., A*, 2005, **284**, 131–137.
15 L. Sun, J. Li, C. L. Wang, S. F. Li, Y. K. Lai, H. B. Chen and C. J. Lin, *J. Hazard. Mater.*, 2009, **171**, 1045–1050.
16 C. L. Wang, M. Y. Wang, K. P. Xie, Q. Wu, L. Sun, Z. Q. Lin and C. J. Lin, *Nanotechnology*, 2011, **22**, 305607.
17 M. Wang, L. Sun, Z. Lin, J. Cai, K. Xie and C. Lin, *Energy Environ. Sci.*, 2013, **6**, 1211–1220.
18 Q. Wu, J. J. Ouyang, K. P. Xiea, L. Sun, M. Y. Wang and C. J. Lin, *J. Hazard. Mater.*, 2012, **199**, 410–417.
19 F. X. Xiao, *J. Phys. Chem. C*, 2012, **116**, 16487–16498.
20 K. P. Xie, L. Sun, C. L. Wang, Y. K. Lai, M. Y. Wang, H. B. Chen and C. J. Lin, *Electrochim. Acta*, 2010, **55**, 7211–7218.
21 K. P. Xie, Q. Wu, Y. Y. Wang, W. X. Guo, M. Y. Wang, L. Sun and C. J. Lin, *Electrochem. Commun.*, 2011, **13**, 1469–1472.
22 H. Li, Z. Bian, J. Zhu, D. Zhang, G. Li, Y. Huo, H. Li and Y. Lu, *J. Am. Chem. Soc.*, 2007, **129**, 8406–8407.
23 Y. Zhao, X. Cao and L. Jiang, *J. Am. Chem. Soc.*, 2007, **129**, 764–765.
24 J. Wang and Z. Lin, *Chem. Mater.*, 2008, **20**, 1257–1261.
25 J. Wang and Z. Lin, *J. Phys. Chem. C*, 2009, **113**, 4026–4030.
26 J. Wang, L. Zhao, V. S.-Y. Lin and Z. Lin, *J. Mater. Chem.*, 2009, **19**, 3682–3687.
27 C. Wang, M. Wang, K. Xie, Q. Wu, L. Sun, Z. Lin and C. Lin, *Nanotechnology*, 2011, **22**, 305607.
28 X. Li, X. Liu, Y. Ma, M. Li, J. Zhao, H. Xin, L. Zhang, Y. Yang, C. Li and Q. Yang, *Adv. Mater.*, 2012, **24**, 1424–1428.
29 M. Ye, H. Y. Liu, C. Lin and Z. Lin, *Small*, 2013, **9**, 312–321.
30 H. G. Yang, G. Liu, S. Z. Qiao, C. H. Sun, Y. G. Jin, S. C. Smith, J. Zou, H. M. Cheng and G. Q. Lu, *J. Am. Chem. Soc.*, 2009, **131**, 4078–4083.
31 K. Zhu, N. R. Neale, A. Miedaner and A. J. Frank, *Nano Lett.*, 2007, **7**, 69–74.
32 K. Zhu, T. B. Vinzant, N. R. Neale and A. J. Frank, *Nano Lett.*, 2007, **7**, 3739–3746.
33 S. P. Albu, A. Ghicov, J. M. Macak, R. Hahn and P. Schmuki, *Nano Lett.*, 2007, **7**, 1286–1289.
34 M. Paulose, K. Shankar, S. Yoriya, H. E. Prakasam, O. K. Varghese, G. K. Mor, T. A. Latempa, A. Fitzgerald and C. A. Grimes, *J. Phys. Chem. B*, 2006, **110**, 16179–16184.
35 R. Beranek, H. Tsuchiya, T. Sugishima, J. M. Macak, L. Taveira, S. Fujimoto, H. Kisch and P. Schmuki, *Appl. Phys. Lett.*, 2005, **87**, 243114.
36 P. Roy, S. Berger and P. Schmuki, *Angew. Chem., Int. Ed.*, 2011, **50**, 2904–2939.
37 U. Diebold, *Appl. Phys. A*, 2003, **76**, 681–687.
38 U. Diebold, *Surf. Sci. Rep.*, 2003, **48**, 53–229.
39 D. Fang, Z. Luo, K. Huang and D. C. Lagoudas, *Appl. Surf. Sci.*, 2011, **257**, 6451–6461.
40 L. Ma and S. Tu, *Environ. Chem. Lett.*, 2011, **9**, 465–472.
41 A. Rivera, K. Tanaka and T. Hisanaga, *Appl. Catal., B*, 1993, **3**, 37–44.
42 X. Q. Chen, X. W. Zhang, Y. L. Su and L. C. Lei, *Appl. Surf. Sci.*, 2008, **254**, 6693–6696.
43 A. Ghicov, J. M. Macak, H. Tsuchiya, J. Kunze, V. Haeublein, L. Frey and P. Schmuki, *Nano Lett.*, 2006, **6**, 1080–1082.
44 J. Lin, R. L. Zong, M. Zhou and Y. F. Zhu, *Appl. Catal., B*, 2009, **89**, 425–431.
45 S. H. Liu, L. X. Yang, S. H. Xu, S. L. Luo and Q. Y. Cai, *Electrochem. Commun.*, 2009, **11**, 1748–1751.
46 N. Lu, X. Quan, J. Li, S. Chen, H. Yu and G. Chen, *J. Phys. Chem. C*, 2007, **111**, 11836–11842.
47 L. Yang, S. Luo, S. Liu and Q. Cai, *J. Phys. Chem. C*, 2008, **112**, 8939–8943.
48 X. S. Zhou, B. Jin, S. S. Zhang, H. J. Wang, H. Yu and F. Peng, *Electrochem. Commun.*, 2012, **19**, 127–130.
49 X. S. Zhou, F. Peng, H. J. Wang, H. Yu and J. A. Yang, *Electrochem. Commun.*, 2011, **13**, 121–124.
50 J. Y. Gong, W. H. Pu, C. Z. Yang and J. D. Zhang, *Electrochim. Acta*, 2012, **68**, 178–183.
51 H. J. Liu, G. G. Liu and Q. X. Zhou, *J. Solid State Chem.*, 2009, **182**, 3238–3242.
52 L. Sun, J. Li, C. L. Wang, S. F. Li, H. B. Chen and C. J. Lin, *Sol. Energy Mater. Sol. Cells*, 2009, **93**, 1875–1880.
53 Z. H. Xu and J. G. Yu, *Nanoscale*, 2011, **3**, 3138–3144.
54 H. Chen, S. Chen, X. Quan, H. T. Yu, H. M. Zhao and Y. B. Zhang, *J. Phys. Chem. C*, 2008, **112**, 9285–9290.
55 Y. K. Lai, H. F. Zhuang, K. P. Xie, D. G. Gong, Y. X. Tang, L. Sun, C. J. Lin and Z. Chen, *New J. Chem.*, 2010, **34**, 1335–1340.
56 Y. Wu, H. Liu, J. Zhang and F. Chen, *J. Phys. Chem. C*, 2009, **113**, 14689–14695.
57 F. X. Xiao, *Chem. Commun.*, 2012, **48**, 6538–6540.
58 L. X. Yang, D. M. He, Q. Y. Cai and C. A. Grimes, *J. Phys. Chem. C*, 2007, **111**, 8214–8217.
59 M. Ye, J. Gong, Y. Lai, C. Lin and Z. Lin, *J. Am. Chem. Soc.*, 2012, **134**, 15720–15723.

60 H. B. Yu, X. H. Wang, H. W. Sun and M. X. Huo, *J. Hazard. Mater.*, 2010, **184**, 753–758.
61 Z. H. Zhang, L. B. Zhang, M. N. Hedhili, H. N. Zhang and P. Wang, *Nano Lett.*, 2013, **13**, 14–20.
62 Y. Hou, X. Y. Li, Q. D. Zhao, X. Quan and G. H. Chen, *Adv. Funct. Mater.*, 2010, **20**, 2165–2174.
63 W. T. Sun, Y. Yu, H. Y. Pan, X. F. Gao, Q. Chen and L. M. Peng, *J. Am. Chem. Soc.*, 2008, **130**, 1124–1125.
64 C. L. Wang, L. Sun, H. Yun, J. Li, Y. K. Lai and C. J. Lin, *Nanotechnology*, 2009, **20**, 295601.
65 L. X. Yang, S. L. Luo, Y. Li, Y. Xiao, Q. Kang and Q. Y. Cai, *Environ. Sci. Technol.*, 2010, **44**, 7641–7646.
66 J. M. Macak, M. Zlamal, J. Krysa and P. Schmuki, *Small*, 2007, **3**, 300–304.
67 G. K. Mor, O. K. Varghese, M. Paulose, K. Shankar and C. A. Grimes, *Sol. Energy Mater. Sol. Cells*, 2006, **90**, 2011–2075.
68 G. Williams, B. Seger and P. V. Kamat, *ACS Nano*, 2008, **2**, 1487–1491.
69 M. R. Hoffmann, S. T. Martin, W. Choi and D. W. Bahnemann, *Chem. Rev.*, 1995, **95**, 69–96.
70 H. Kisch, *Angew. Chem., Int. Ed.*, 2013, **52**, 812–847.
71 R. W. Matthews, *J. Catal.*, 1988, **113**, 549–555.
72 J. Krýsa, G. Waldner, H. Měšťánková, J. Jirkovský and G. Grabner, *Appl. Catal., B*, 2006, **64**, 290–301.
73 H. F. Zhuang, C. J. Lin, Y. K. Lai, L. Sun and J. Li, *Environ. Sci. Technol.*, 2007, **41**, 4735–4740.
74 Y. K. Lai, H. F. Zhuang, L. Sun, Z. Chen and C. J. Lin, *Electrochim. Acta*, 2009, **54**, 6536–6542.
75 J. G. Yu and B. Wang, *Appl. Catal., B*, 2010, **94**, 295–302.
76 J. M. Macak and P. Schmuki, *Electrochim. Acta*, 2006, **52**, 1258–1264.
77 S. Bauer, S. Kleber and P. Schmuki, *Electrochem. Commun.*, 2006, **8**, 1321–1325.
78 J. G. Yu, G. P. Dai and B. Cheng, *J. Phys. Chem. C*, 2010, **114**, 19378–19385.
79 X. J. Xu, X. S. Fang, T. Y. Zhai, H. B. Zeng, B. D. Liu, X. Y. Hu, Y. Bando and D. Golberg, *Small*, 2011, **7**, 445–449.
80 R. Asahi, Y. Taga, W. Mannstadt and A. Freeman, *Phys. Rev. B: Condens. Matter Mater. Phys.*, 2000, **61**, 7459.
81 Y. K. Lai, J. Y. Huang, H. F. Zhang, V. P. Subramaniam, Y. X. Tang, D. G. Gong, L. Sundar, L. Sun, Z. Chen and C. J. Lin, *J. Hazard. Mater.*, 2010, **184**, 855–863.
82 J. S. Wang, Z. Z. Wang, H. Y. Li, Y. T. Cui and Y. C. Du, *J. Alloys Compd.*, 2010, **494**, 372–377.
83 J. J. Xu, Y. H. Ao, M. D. Chen and D. G. Fu, *Appl. Surf. Sci.*, 2010, **256**, 4397–4401.
84 X. Liu, Z. Q. Liu, J. Zheng, X. Yan, D. D. Li, S. Chen and W. Chu, *J. Alloys Compd.*, 2011, **509**, 9970–9976.
85 G. T. Yan, M. Zhang, J. Hou and J. J. Yang, *Mater. Chem. Phys.*, 2011, **129**, 553–557.
86 D. Chen, D. Yang, Q. Wang and Z. Jiang, *Ind. Eng. Chem. Res.*, 2006, **45**, 4110–4116.
87 J. Y. Li, N. Lu, X. Quan, S. Chen and H. M. Zhao, *Ind. Eng. Chem. Res.*, 2008, **47**, 3804–3808.
88 N. Lu, H. M. Zhao, J. Y. Li, X. Quan and S. Chen, *Sep. Purif. Technol.*, 2008, **62**, 668–673.
89 G. Liu, C. Sun, L. Cheng, Y. Jin, H. Lu, L. Wang, S. C. Smith, G. Q. Lu and H.-M. Cheng, *J. Phys. Chem. C*, 2009, **113**, 12317–12324.
90 J. J. Yuan, H. D. Li, S. Y. Gao, Y. H. Lin and H. Y. Li, *Chem. Commun.*, 2010, **46**, 3119–3121.
91 D. Li, N. Ohashi, S. Hishita, T. Kolodiazhnyi and H. Haneda, *J. Solid State Chem.*, 2005, **178**, 3293–3302.
92 Y. L. Su, X. W. Zhang, S. Han, X. Q. Chen and L. C. Lei, *Electrochem. Commun.*, 2007, **9**, 2291–2298.
93 Y. L. Su, X. W. Zhang, M. H. Zhou, S. Han and L. C. Lei, *J. Photochem. Photobiol., A*, 2008, **194**, 152–160.
94 J. C. Yu, L. Zhang, Z. Zheng and J. Zhao, *Chem. Mater.*, 2003, **15**, 2280–2286.
95 Z. Q. Liu, X. Yan, W. Chu and D. D. Li, *Appl. Surf. Sci.*, 2010, **257**, 1295–1299.
96 Y. Y. Zhang, W. Y. Fu, H. B. Yang, S. K. Liu, P. Sun, M. X. Yuan, D. Ma, W. Y. Zhao, Y. M. Sui, M. H. Li and Y. X. Li, *Thin Solid Films*, 2009, **518**, 99–103.
97 J. J. Xu, Y. H. Ao, M. D. Chen and D. G. Fu, *Appl. Surf. Sci.*, 2010, **256**, 4397–4401.
98 Z. M. El-Bahy, A. A. Ismail and R. M. Mohamed, *J. Hazard. Mater.*, 2009, **166**, 138–143.
99 W. P. Qin, D. S. Zhang, D. Zhao, L. L. Wang and K. Z. Zheng, *Chem. Commun.*, 2010, **46**, 2304–2306.
100 Y. Tang, W. Di, X. Zhai, R. Yang and W. Qin, *ACS Catal.*, 2013, **3**, 405–412.
101 A.-W. Xu, Y. Gao and H.-Q. Liu, *J. Catal.*, 2002, **207**, 151–157.
102 J. W. Shi, J. T. Zheng and P. Wu, *J. Hazard. Mater.*, 2009, **161**, 416–422.
103 M. Zhou, J. Yu and B. Cheng, *J. Hazard. Mater.*, 2006, **137**, 1838–1847.
104 L. Q. Jing, B. F. Xin, F. L. Yuan, L. P. Xue, B. Q. Wang and H. G. Fu, *J. Phys. Chem. B*, 2006, **110**, 17860–17865.
105 M. Ni, M. K. H. Leung, D. Y. C. Leung and K. Sumathy, *Renewable Sustainable Energy Rev.*, 2007, **11**, 401–425.
106 T. Umebayashi, T. Yamaki, H. Itoh and K. Asai, *J. Phys. Chem. Solids*, 2002, **63**, 1909–1920.
107 J. F. Zhu, F. Chen, J. L. Zhang, H. J. Chen and M. Anpo, *J. Photochem. Photobiol., A*, 2006, **180**, 196–204.
108 J. Zhu, W. Zheng, B. He, J. Zhang and M. Anpo, *J. Hazard. Mater.*, 2004, **216**, 35–43.
109 S. M. Chang and R. A. Doong, *J. Phys. Chem. B*, 2006, **110**, 20808–20814.
110 J. Lukáč, M. Klementová, P. Bezdička, S. Bakardjieva, J. Šubrt, L. Szatmáry, Z. Bastl and J. Jirkovský, *Appl. Catal., B*, 2007, **74**, 83–91.
111 H. J. Liu, G. G. Liu and X. Y. Shi, *oids Surf., A*, 2010, **363**, 35–40.
112 S. Liu, Z. Qu, X. Han and C. Sun, *Catal. Today*, 2004, **93**, 877–884.
113 I. Paramasivalm, J. M. Macak and P. Schmuki, *Electrochem. Commun.*, 2008, **10**, 71–75.
114 X. L. He, Y. Y. Cai, H. M. Zhang and C. H. Liang, *J. Mater. Chem.*, 2011, **21**, 475–480.

115 Y. H. Tang, S. L. Luo, Y. R. Teng, C. B. Liu, X. L. Xu, X. L. Zhang and L. Chen, *J. Hazard. Mater.*, 2012, **241**, 323–330.
116 Z. W. Seh, S. H. Liu, M. Low, S. Y. Zhang, Z. L. Liu, A. Mlayah and M. Y. Han, *Adv. Mater.*, 2012, **24**, 2310–2314.
117 S. C. Warren and E. Thimsen, *Energy Environ. Sci.*, 2012, **5**, 5133–5146.
118 Z. Bian, J. Zhu, F. Cao, Y. Lu and H. Li, *Chem. Commun.*, 2009, 3789–3791.
119 Y. L. Su and Y. R. Deng, *Appl. Surf. Sci.*, 2011, **257**, 9791–9795.
120 T. T. Isimjan, H. Kazemian, S. Rohani and A. K. Ray, *J. Mater. Chem.*, 2010, **20**, 10241–10245.
121 M. Ye, J. Gong, Y. Lai, C. Lin and Z. Lin, *J. Am. Chem. Soc.*, 2012, **134**, 15720–15723.
122 Z. Zhang, Y. Yu and P. Wang, *ACS Appl. Mater. Interfaces*, 2012, **4**, 990–996.
123 S. K. Mohapatra, N. Kondamudi, S. Banerjee and M. Misra, *Langmuir*, 2008, **24**, 11276–11281.
124 H. B. Yu, X. H. Wang, H. W. Sun and M. X. Huo, *J. Hazard. Mater.*, 2010, **184**, 753–758.
125 S. Y. Chang, S. F. Chen and Y. C. Huang, *J. Phys. Chem. C*, 2011, **115**, 1600–1607.
126 Z. Q. Lin, Y. K. Lai, R. G. Hu, J. Li, R. G. Du and C. J. Lin, *Electrochim. Acta*, 2010, **55**, 8717–8723.
127 M. Wang, L. Sun, Z. Lin, J. Cai, K. Xie and C. Lin, *Energy Environ. Sci.*, 2013, **6**, 1211–1220.
128 Y. N. Zhang, G. H. Zhao, Y. Z. Lei, P. Q. Li, M. F. Li, Y. N. Jin and B. Y. Lv, *ChemPhysChem*, 2010, **11**, 3491–3498.
129 C. L. Wang, L. Sun, K. P. Xie and C. J. Lin, *Sci. China, Ser. B: Chem.*, 2009, **52**, 2148–2155.
130 Y. Xie, G. Ali, S. H. Yoo and S. O. Cho, *ACS Appl. Mater. Interfaces*, 2010, **2**, 2910–2914.
131 G. S. Li, L. Wu, F. Li, P. P. Xu, D. Q. Zhang and H. X. Li, *Nanoscale*, 2013, **5**, 2118–2125.
132 S. C. Hayden, N. K. Allam and M. A. El-Sayed, *J. Am. Chem. Soc.*, 2010, **132**, 14406–14408.
133 X. W. Zhang, L. C. Lei, J. L. Zhang, Q. X. Chen, J. G. Bao and B. Fang, *Sep. Purif. Technol.*, 2009, **66**, 417–421.
134 Q. Y. Wang, X. C. Yang, D. Liu, L. N. Chi and J. W. Hou, *Electrochim. Acta*, 2012, **83**, 140–145.
135 W. Wilson, A. Manivannan and V. R. Subramanian, *Appl. Catal., A*, 2012, **441**, 1–9.
136 L. X. Yang, S. L. Luo, R. H. Liu, Q. Y. Cai, Y. Xiao, S. H. Liu, F. Su and L. F. Wen, *J. Phys. Chem. C*, 2010, **114**, 4783–4789.
137 M. Gutierrez and J. Ortega, *J. Electrochem. Soc.*, 1989, **136**, 2316–2320.
138 J. L. Ouyang, M. L. Chang, Y. Y. Zhang and X. J. Li, *Thin Solid Films*, 2012, **520**, 2994–2999.
139 H. Feng, T. T. Tran, L. Chen, L. J. Yuan and Q. Y. Cai, *Chem. Eng. J.*, 2013, **215**, 591–599.
140 Y.-G. Zhang, L.-L. Ma, J.-L. Li and Y. Yu, *Environ. Sci. Technol.*, 2007, **41**, 6264–6269.
141 J. L. Li, L. Liu, Y. Yu, Y. W. Tang, H. L. Li and F. P. Du, *Electrochem. Commun.*, 2004, **6**, 940–943.
142 Y. Hou, X. Y. Li, X. J. Zou, X. Quan and G. C. Chen, *Environ. Sci. Technol.*, 2009, **43**, 858–863.
143 H. Y. Li, J. S. Wang, X. Chen, M. L. Zhou, G. S. Sun, K. L. Huang and Q. N. Guo, *Chin. J. Inorg. Chem.*, 2010, **26**, 217–222.
144 J. Wang, G. Ji, Y. Liu, M. A. Gondal and X. Chang, *Catal. Commun.*, 2014, **46**, 17–21.
145 S. Zhang, S. Zhang, F. Peng, H. Zhang, H. Liu and H. Zhao, *Electrochem. Commun.*, 2011, **13**, 861–864.
146 A. Murphy, P. Barnes, L. Randeniya, I. Plumb, I. Grey, M. Horne and J. Glasscock, *Int. J. Hydrogen Energy*, 2006, **31**, 1999–2017.
147 A. I. Kontos, V. Likodimos, T. Stergiopoulos, D. S. Tsoukleris, P. Falaras, I. Rabias, G. Papavassiliou, D. Kim, J. Kunze and P. Schmuki, *Chem. Mater.*, 2009, **21**, 662–672.
148 C. Frandsen, C. R. H. Bahl, B. Lebech, K. Lefmann, L. T. Kuhn, L. Keller, N. H. Andersen, M. v. Zimmermann, E. Johnson and S. N. Klausen, *Phys. Rev. B: Condens. Matter Mater. Phys.*, 2005, **72**, 214406.
149 Y. Q. Cong, Z. Li, Y. Zhang, Q. Wang and Q. Xu, *Chem. Eng. J.*, 2012, **191**, 356–363.
150 J. Bandara and H. Weerasinghe, *Sol. Energy Mater. Sol. Cells*, 2005, **85**, 385–390.
151 J. Guo, W. Y. Fu, H. B. Yang, Q. J. Yu, W. Y. Zhao, X. M. Zhou, Y. M. Sui, J. A. Ding, Y. G. Li, S. L. Cheng and M. H. Li, *J. Phys. D: Appl. Phys.*, 2010, **43**, 245202.
152 N. K. Shrestha, M. Yang, Y. C. Nah, I. Paramasivam and P. Schmuki, *Electrochem. Commun.*, 2010, **12**, 254–257.
153 L. C. Sim, K. W. Ng, S. Ibrahim and P. Saravanan, *Int. J. Photoenergy*, 2013, 659013.
154 M. Hasnat, M. Uddin, A. Samed, S. Alam and S. Hossain, *J. Hazard. Mater.*, 2007, **147**, 471–477.
155 O. Fouad, A. Ismail, Z. Zaki and R. Mohamed, *Appl. Catal., B*, 2006, **62**, 144–149.
156 Y. Z. Lei, G. H. Zhao, M. C. Liu, Z. N. Zhang, X. L. Tong and T. C. Cao, *J. Phys. Chem. C*, 2009, **113**, 19067–19076.
157 Z. H. Zhang, Y. Yuan, L. H. Liang, Y. X. Cheng, G. Y. Shi and L. T. Jin, *J. Hazard. Mater.*, 2008, **158**, 517–522.
158 H. Y. Yang, S. F. Yu, S. P. Lau, X. W. Zhang, D. D. Sun and G. Jun, *Small*, 2009, **5**, 2260–2264.
159 F. X. Xiao, *ACS Appl. Mater. Interfaces*, 2012, **4**, 7054–7062.
160 Y. C. Huang, S. Y. Chang, C. F. Lin and W. J. J. Tseng, *J. Mater. Chem.*, 2011, **21**, 14056–14061.
161 P. Li, G. Zhao, M. Li, T. Cao, X. Cui and D. Li, *Appl. Catal., B*, 2012, **111**, 578–585.
162 P. Q. Li, G. H. Zhao, M. F. Li, T. C. Cao, X. Cui and D. M. Li, *Appl. Catal., B*, 2012, **111**, 578–585.
163 A. Babar, S. Shinde, A. Moholkar, C. Bhosale, J. Kim and K. Rajpure, *J. Alloys Compd.*, 2011, **509**, 3108–3115.
164 P. Q. Li, G. H. Zhao, X. Cui, Y. G. Zhang and Y. T. Tang, *J. Phys. Chem. C*, 2009, **113**, 2375–2383.
165 S. Chai, G. Zhao, P. Li, Y. Lei, Y.-n. Zhang and D. Li, *J. Phys. Chem. C*, 2011, **115**, 18261–18269.
166 T. L. Li and H. Teng, *J. Mater. Chem.*, 2010, **20**, 3656–3664.
167 R. H. Liu, Y. T. Liu, C. B. Liu, S. L. Luo, Y. R. Teng, L. X. Yang, R. B. Yang and Q. Y. Cai, *J. Alloys Compd.*, 2011, **509**, 2434–2440.

168 X. Y. Li, Y. Hou, Q. D. Zhao and G. H. Chen, *Langmuir*, 2011, **27**, 3113–3120.
169 G. G. Liu, X. Z. Zhang, Y. J. Xu, X. S. Niu, L. Q. Zheng and X. J. Ding, *Chemosphere*, 2004, **55**, 1287–1291.
170 C. Ping, L. Wei, T. L. Zhou, Y. P. Jin and M. Y. Gu, *J. Photochem. Photobiol., A*, 2004, **168**, 97–101.
171 M. A. Valenzuela, P. Bosch, J. Jimenez-Becerrill, O. Quiroz and A. I. Paez, *J. Photochem. Photobiol., A*, 2002, **148**, 177–182.
172 S. Xu, D. Feng and W. Shangguan, *J. Phys. Chem. C*, 2009, **113**, 2463–2467.
173 Z. H. Yuan and L. D. Zhang, *J. Mater. Chem.*, 2001, **11**, 1265–1268.
174 Y. Hou, X. Y. Li, Q. D. Zhao, X. Quan and G. H. Chen, *Environ. Sci. Technol.*, 2010, **44**, 5098–5103.
175 M. Wang, L. Sun, J. Cai, P. Huang, Y. Su and C. Lin, *J. Mater. Chem. A*, 2013, **1**, 12082–12087.
176 D. Y. Pan, C. Xi, Z. Li, L. Wang, Z. W. Chen, B. Luc and M. H. Wu, *J. Mater. Chem. A*, 2013, **1**, 3551–3555.
177 J. Lin, R. L. Zong, M. Zhou and Y. F. Zhu, *Appl. Catal., B*, 2009, **89**, 425–431.
178 C. B. Liu, Y. R. Teng, R. H. Liu, S. L. Luo, Y. H. Tang, L. Y. Chen and Q. Y. Cai, *Carbon*, 2011, **49**, 5312–5320.
179 P. Song, X. Zhang, M. Sun, X. Cui and Y. Lin, *Nanoscale*, 2012, **4**, 1800–1804.
180 K. S. Novoselov, A. K. Geim, S. Morozov, D. Jiang, Y. Zhang, S. Dubonos, I. Grigorieva and A. Firsov, *Science*, 2004, **306**, 666–669.
181 P. Song, X. Y. Zhang, M. X. Sun, X. L. Cui and Y. H. Lin, *Nanoscale*, 2012, **4**, 1800–1804.
182 D. Y. Pan, C. Xi, Z. Li, L. Wang, Z. W. Chen, B. Luc and M. H. Wu, *J. Mater. Chem. A*, 2013, **1**, 3551–3555.
183 J. Gu, Y. Yan, J. W. Krizan, Q. D. Gibson, Z. M. Detweiler, R. J. Cava and A. B. Bocarsly, *J. Am. Chem. Soc.*, 2014, **136**, 830–833.

